



The LSST Era of Supermassive Black Hole Accretion Disk Reverberation Mapping

Andjelka B. Kovačević^{1,2}, Viktor Radović¹, Dragana Ilić^{1,3}, Luka Č. Popović^{1,4}, Roberto J. Assef⁵, Paula Sánchez-Sáez^{6,7}, Robert Nikutta⁸, Claudia M. Raiteri⁹, Ilsang Yoon¹⁰, Yasaman Homayouni¹¹, Yan-Rong Li¹², Neven Caplar¹³, Božena Czerny¹⁴, Swayamtrupta Panda^{14,15,16}, Claudio Ricci^{17,18}, Isidora Jankov¹, Hermine Landt¹⁹, Christian Wolf^{20,21}, Jelena Kovačević-Dojčinović⁴, Maša Lakićević⁴, Đorđe V. Savić^{4,22}, Oliver Vince⁴, Saša Simić²³, Iva Čvorović-Hajdinjak¹, and Sladjana Marčeta-Mandić⁴

¹ University of Belgrade-Faculty of Mathematics, Department of Astronomy, Studentski trg 16, Belgrade, Serbia; andjelka@matf.bg.ac.rs

² PIFI Research Fellow, Key Laboratory for Particle Astrophysics, Institute of High Energy Physics, Chinese Academy of Sciences, 19B Yuquan Road, 100049 Beijing, People's Republic of China

³ Hamburger Sternwarte, Universität Hamburg, Gojenbergsweg 112, D-21029 Hamburg, Germany

⁴ Astronomical Observatory, Volgina 7, 11000 Belgrade, Serbia

⁵ Núcleo de Astronomía de la Facultad de Ingeniería y Ciencias, Universidad Diego Portales, Av. Ejército Libertador 441, Santiago, Chile

⁶ Directorate for Science, European Southern Observatory, Karl-Schwarzschild-Strasse 2, Garching bei München, Germany

⁷ Millennium Institute of Astrophysics (MAS), Nuncio Monseñor Sótero Sanz 100, Providencia, Santiago, Chile

⁸ NSF's NOIRLab, 950 N. Cherry Avenue, Tucson, AZ 85719, USA

⁹ INAF-Osservatorio Astrofisico di Torino, Via Osservatorio 20, I-10025 Pino Torinese, Italy

¹⁰ The National Radio Astronomy Observatory, 520 Edgemont Road, Charlottesville, VA 22903, USA

¹¹ The Pennsylvania State University, 201 Old Main, University Park, PA 16802, USA

¹² Key Laboratory for Particle Astrophysics, Institute of High Energy Physics, Chinese Academy of Sciences, 19B Yuquan Road, Beijing 100049, People's Republic of China

¹³ Astrophysical Department, Princeton University, 4 Ivy Lane, Princeton, NJ, USA

¹⁴ Center for Theoretical Physics, Polish Academy of Sciences, Al. Lotnikow 32/46, 02-668 Warsaw, Poland

¹⁵ Nicolaus Copernicus Astronomical Center, Polish Academy of Sciences, ul. Bartycka 18, 00-716 Warsaw, Poland

¹⁶ Laboratório Nacional de Astrofísica—MCTIC, R. dos Estados Unidos, 154—Nações, Itajubá—MG, 37504-364, Brazil

¹⁷ Núcleo de Astronomía de la Facultad de Ingeniería, Universidad Diego Portales, Av. Ejército Libertador 441, Santiago, Chile

¹⁸ Kavli Institute for Astronomy and Astrophysics, Peking University, Beijing 100871, People's Republic of China

¹⁹ Centre for Extragalactic Astronomy, Department of Physics, Durham University, South Road, Durham DH1 3LE, UK

²⁰ Research School of Astronomy and Astrophysics, Australian National University, Weston Creek, ACT 2611, Australia

²¹ Centre for Gravitational Astrophysics, Australian National University, Canberra, ACT 2600, Australia

²² Institut d'Astrophysique et de Géophysique, Université de Liège, Allée du 6 Août 19c, 4000 Liège, Belgium

²³ Faculty of Science, University of Kragujevac, Radoja Domanovića 12, 34000 Kragujevac, Serbia

Received 2022 April 1; revised 2022 August 8; accepted 2022 August 9; published 2022 October 3

Abstract


The Vera C. Rubin Observatory's Legacy Survey of Space and Time (LSST) will detect an unprecedentedly large sample of actively accreting supermassive black holes with typical accretion disk (AD) sizes of a few light days. This brings us to face challenges in the reverberation mapping (RM) measurement of AD sizes in active galactic nuclei using interband continuum delays. We examine the effect of LSST cadence strategies on AD RM using our metric `AGN_TimeLagMetric`. It accounts for redshift, cadence, the magnitude limit, and magnitude corrections for dust extinction. Running our metric on different LSST cadence strategies, we produce an atlas of the performance estimations for LSST photometric RM measurements. We provide an upper limit on the estimated number of quasars for which the AD time lag can be computed within $0 < z < 7$ using the features of our metric. We forecast that the total counts of such objects will increase as the mean sampling rate of the survey decreases. The AD time lag measurements are expected for >1000 sources in each deep drilling field (DDF; (10 deg^2)) in any filter, with the redshift distribution of these sources peaking at $z \approx 1$. We find the LSST observation strategies with a good cadence ($\lesssim 5$ days) and a long cumulative season (~ 9 yr), as proposed for LSST DDF, are favored for the AD size measurement. We create synthetic LSST light curves for the most suitable DDF cadences and determine RM time lags to demonstrate the impact of the best cadences based on the proposed metric.

Unified Astronomy Thesaurus concepts: Quasars (1319); Accretion (14); Time domain astronomy (2109); Reverberation mapping (2019)

1. Introduction

The first Event Horizon Telescope (EHT; Event Horizon Telescope Collaboration et al. 2019) observations of M87 revealed a prominent ring of $\sim 40 \mu\text{as}$ in diameter, compatible with a lensed photon ring encircling the shadow of a supermassive black hole (SMBH). This iconic image, in fact,

portrays the accretion disk (AD) surrounding the SMBH. As a result, we are now closer than ever to constructing a definitive model of accretion disks. Inflowing gas quickly accretes from a few parsecs down to a few Schwarzschild radii of the SMBH forming a ring-like structure (the AD) that characterizes the phenomenon of an active galactic nucleus (AGN). There is only a short (~ 2 Myr) active phase²⁴ for these objects, followed by prolonged periods of inactivity (see Anglés-

 Original content from this work may be used under the terms of the [Creative Commons Attribution 4.0 licence](https://creativecommons.org/licenses/by/4.0/). Any further distribution of this work must maintain attribution to the author(s) and the title of the work, journal citation and DOI.

²⁴ For luminous quasars, the activity period can be of the order of 10 Myr (e.g., Hopkins et al. 2005).

Alcázar et al. 2021)²⁵. In addition to theoretical investigations, a variety of activity cycles have been observed in radio and optical active galactic nuclei (AGNs). The longest timescales of 10^7 – 10^8 yr have been traced using radio wavelengths, and short timescales of 10^4 – 10^5 yr (and down to years) have been estimated using radio wavelengths ($\sim 10^6$ yr; Biava et al. 2021), radio and optical wavelengths (central engine already quiescent, but the remnant of the past activity is on scales of $\sim 10^4$ yr; Morganti 2017; Ichikawa et al. 2019; review of multiple cycles), and optical wavelengths (e.g., changing look AGNs where the continuum changes over a timescale of years; Kollatschny & Fricke 1985; Oknyansky et al. 2019; Ilić et al. 2020; Panda 2022). A recent review on the AGN active phase timescales is reported by Moravec et al. (2022).

The most luminous AGNs, known as quasars (Matthews & Sandage 1963; Schmidt 1963), are thought to be SMBHs accreting matter at high rates through accretion disks that are both geometrically thin and optically thick (Sun & Malkan 1989). In contrast, most AGNs in the local universe²⁶, such as the one in M87, correspond to SMBHs fed by hot plasma at significantly lower accretion rates than quasars (Ichimaru 1977; Blandford & Begelman 1999; Yuan & Narayan 2014).

We already have a typical several-component model of AGNs that includes the AD, broad-line region (BLR), corona, molecular torus, narrow-line region, and jets, and that captures the observed features of spectral energy distributions for AGNs. Nevertheless, the precise geometry and behavior of these components are mostly unknown (for a review, see Padovani et al. 2017). Even though the entirety of the large-scale structure has been identified, the features of the central engine are unclear due to its small dimensions, even for the nearest AGNs. As a result, additional information must be gathered indirectly, through the comparison of theoretical model predictions and observations. Recent developments in instrumentation have allowed the BLR to be spatially resolved in the case of nearby active galaxies (Gravity Collaboration et al. 2018; Event Horizon Telescope Collaboration et al. 2019). However, at least in the near future, it will be difficult to resolve a significant sample of more distant AGNs. Fortunately, the SMBH AD may be examined using either microlensing studies of gravitationally lensed quasars to determine the accretion disk’s half light radii at different wavelengths (Morgan et al. 2012; MacLeod et al. 2015), or reverberation mapping (RM) investigations of the SMBH’s immediate surroundings (Blandford & McKee 1982). RM offers information on the structure and kinematics of the BLR and accretion disk (see early works of Cherepashchuk & Lyutiy 1973; Gaskell & Sparke 1986) in the time domain. According to the RM premises, the main driver of fluctuations in the BLR lines is accretion disk emission variability. Observing the time delays between disk and broad-line emission can be used to calculate the BLR dimension, which in turn allows us to estimate the SMBH mass. More than 100 robust dynamical black hole mass estimates have been published in the literature, slowly building up to a statistically significant sample (Kaspi et al. 2000; Peterson et al. 2004; Du et al. 2015; Panda et al. 2019; Thater et al. 2019).

²⁵ Continuous accretion is proposed to cope with the demands of growing black holes in the early universe (Zubovas & King 2021).

²⁶ We denote as “local universe” the regions within 300 Mpc ($z < 0.1$) from Earth (Tekhanovich & Baryshev 2016).

The Shakura & Sunyaev (1973) model was the first to provide a more comprehensive picture of an optically thick, geometrically thin accretion disk, albeit in the context of stellar-mass black holes. Soon, Galeev et al. (1979) proposed magnetic reconnection in a corona above a Shakura & Sunyaev (1973) disk to explain the hard X-ray emission observed in AGNs. The central corona can directly illuminate and heat the outer AGN disk (e.g., Frank et al. 2002), resulting in the “lampost/reprocessing” paradigm²⁷. According to this hypothesis, the fluctuating X-ray energy from the corona can be reprocessed and detected in the UV/optical light from the disk.

Also, Sahu et al. (2019a) and Sahu et al. (2019b) proposed a relation between SMBH mass and central velocity dispersion that is dependent on morphological type, capable of more precisely estimating SMBH masses in other galaxies, and has implications for calibrating virial f-factors. Similarly to the case of the BLR, the light travel time across the AD can be inferred through RM time delays (see, e.g., Collier et al. 1998). In particular, in classic AD theory, effective temperature is coupled to black hole mass and accretion rate (Cackett et al. 2007; Liu et al. 2008; Morgan et al. 2010; Fausnaugh et al. 2016; Panda et al. 2018). When compared to the outer and cooler AD regions, the reprocessing model demonstrates that radiation from the innermost part of the accretion disk, closer to the SMBH, has a peak of emission at shorter wavelengths, and its variability is detected (Cackett et al. 2007; Chelouche 2013; Edelson et al. 2015) with a mean delay scaling $\tau \sim \lambda^{4/3}$ (Collier et al. 1998; Starkey et al. 2016). An alternate AGN variability model proposed by Dexter & Agol (2011) assumes large local temperature fluctuations in the AD as the origin of flux variability. While it can explain the amplitude and timescales of observed variability (MacLeod et al. 2010), it cannot explain the wavelength dependence of the time lags (Starkey et al. 2016). Yu et al. (2022) modeled AGN variability as a damped harmonic oscillator and offer more insight; the modeled short-term variability behaves differently in the vicinity of 2500Å, which could be an imprint of a different accretion flow geometry rather than a homogeneous thin disk.

While thin ADs are the most robust explanation for AGN luminosity and variability, multiple studies have found that the AD sizes depart from the immediate prediction of the model. Estimated accretion disk sizes from RM campaigns are three times larger than those expected based on thin-disk theory (Sergeev et al. 2005; Shappee et al. 2014; Edelson et al. 2015; Fausnaugh et al. 2016; Jiang et al. 2017; Cackett et al. 2018; Mudd et al. 2018). Noticeably, microlensing studies of luminous lensed quasars have independently obtained comparable conclusions (Pooley et al. 2006, 2007; Morgan et al. 2010; Mosquera et al. 2013; Chartas et al. 2016).

Using data from the Neil Gehrels Swift Observatory (see Edelson et al. 2019), Shappee et al. (2014) and McHardy et al. (2014) found that the UV leads the optical emission in NGC 2617 and NGC 5548, respectively. Following these campaigns, Edelson et al. (2017) and Edelson et al. (2019) observed four AGNs (NGC 5548, NGC 4151, NGC 4593, and Mrk 509) and found significantly correlated UV/optical fluctuations, and the same overall pattern of interband delays growing from UV to optical wavelengths. While these lags are two times larger than expected from classical theory, the uncertainties on the

²⁷ Electrons heated by a magnetic field transfer their energy to optical/UV photons and upscatter them into the X band.

predicted lags are large, so it is unclear whether this is inconsistent with the usual thin-disk picture. Using Pan-STARRS light curves, Jiang et al. (2017) measured the continuum lags of ~ 200 quasars (the mean lags between the g band and the r , i , and z bands for the whole sample are 1.1, 2.1, and 3.0 days), whereas Mudd et al. (2018) used the Dark Energy Survey’s (DES’s) photometric data to measure the disk sizes of 15 quasars (e.g., lags ≤ 3.0 days in the r, i band, and ≤ 5.0 days in the z band relative to the g band). Homayouni et al. (2019) recently measured the continuum lags of 95 quasars using photometric data from the Sloan Digital Sky Survey (SDSS) RM project. They found that average size of measured disks is consistent with the Shakura & Sunyaev (1973) analytic thin-disk model. However, it was shown that there is a wide variety of disk sizes, both small and large, that are in excess of the measurement uncertainties.

Yu et al. (2020) assessed the time lags and accretion disk sizes of 22 quasars with SMBH masses ranging from 10^7 to $10^9 M_\odot$ with the data from the DES standard-star fields and the supernova C fields. They concluded that when the disk variability is taken into account, most of the reported accretion disk diameters are compatible with the predictions of the classic thin-disk model. Guo et al. (2022) compiled a sample of 92 AGNs at $z < 0.75$ with gri photometric light curves from the archival data of the Zwicky Transient Facility and found that AD sizes are systematically larger than expected, although the ratio of the measured to theoretical disk sizes depends on using the emissivity—or responsivity—weighted disk radius.

According to a recent study conducted by Kara et al. (2021), short C IV and Ly α delays in the spectra of Mrk 817 show that the accretion disk extends beyond the UV broad-line region. Also, Netzer (2022) suggested that the large bulk of observed continuum delays are due to varying diffuse BLR emission rather than from disk emission (see also Korista & Goad 2001; Lawther et al. 2018).

We are about to enter an era in which an abundance of new data provides the opportunity to settle the disk size dispute and unravel diverse effects. The Vera C. Rubin Observatory opens a window of discovery in our dynamic universe through its Legacy Survey of Space and Time (LSST). The LSST project is intended to investigate dark energy and dark matter, the solar system inventory, the transient optical sky, and to map the Milky Way (see Ivezić et al. 2019). The distribution of revisit times (i.e., the cadence of observations) is among the main constraints on data and system properties placed by the four main science themes (see Ivezić et al. 2019). The LSST community has conducted a thorough investigation of prospective cadences (Connolly et al. 2014). Metrics developed by the LSST community provide a scientific testbed for evaluating a suite of cadence simulations (see details in Bianco et al. 2022) employing the Metrics Analysis Framework (MAF; Jones et al. 2014, 2020) and The Operations Simulator (OpSim; Reuter et al. 2016). Both codes are open source. The OpSim generates databases containing 10 yr pointing histories, complete with weather, seeing, and sky brightness information. It is more often now known as the Feature Based Scheduler (or FBS), and its fifth version is used for this analysis. The MAF offers an application programming interface for inferring image properties (e.g., seeing, proper motion) over various spatial scales, as well as tools for predicting the properties of photometric measurements for objects and light curves inserted in survey simulations (see details in Bianco et al. 2022). LSST

is expected to tightly constrain the radial dependence of the effective temperature in accretion disks through its u, g, r, i, z, y light curves with daily cadences of a large sample of AGNs (see details in the AGN SC Roadmap by Shemmer et al. 2018). Assuming a 5σ depth of 24.6 mag in the r band, De Cicco et al. (2021) estimated a sky density of 6.2×10^6 AGNs for the LSST main survey of $\sim 18,000$ deg 2 . Specific metrics on the number of quasars that will be detected in the 10 yr coadded i -band observations as a function of OpSim run have been developed by Assef et al. (2021a).

The LSST AGN and Transient and Variable Stars (TVS) Scientific Collaborations devised a variety of metrics²⁸ to quantify the impact of LSST observing strategies on different variability and photometric redshift measurements as well as quasar counts. The Blazar Variability metric by Raiteri et al. (2022) evaluates the performance of LSST observing strategies for extracting information from data linked to the shortest time and spatial scales of blazars (less than 1 hr to years). Related to largest scales, Assef et al. (2021b, 2021a) developed two metrics to evaluate the 10 yr coadded depths expected for each band in the context of photometric redshifts for type-1 quasars. Yu & Richards (2021) created a model-independent metric that quantifies the degree to which we can deduce the structure function of variable sources (e.g., AGNs) observed by LSST. The metric described in the following sections complements this suite by quantifying the impact of LSST observing strategies on the AD and BLR photometric RM, covering timescales from a few up to 400 lt-days. In addition, as LSST will be able to measure AGN dust sublimation radii the recovery of which critically depends on the cadence as well as the continuity of observations (see Hönig 2014), our metric could be applied on the corresponding timescales of several tens of days. The caveat, however, is that if most accretion disks dominate the AGN emission in the near-IR (see, e.g., Landt et al. 2011), the dust sublimation radius reverberation signal will be difficult to isolate.

Kovačević et al. (2021b) developed a metric to assess the impact of different LSST cadences on the detection of periodicity and time lags for AGNs. While modeling specific object classes is useful for assessing the science implications, they may not cover the entire discovery space. When paired with survey design, metrics that provide quantized estimates rather than continuous probability distributions can be useful for survey design optimization (Bellm et al. 2022).

Based on the AGN SC roadmap premises as well as a need for metrics, the goal of this work is to evaluate different LSST cadences for the science case of measuring AGN interband time delays, specifically in the deep drilling fields (DDFs), and to identify suboptimal cadences. The LSST DDFs will have the deepest coadded depths of the survey (see Brandt et al. 2018), and are expected to exceed those achieved by 8 m class observatories in the same areas (see Aihara et al. 2022). Roughly 10%–20% of the LSST observing time will be used in mini-surveys and in the six DDFs. Through a combination of depth and cadence, the DDFs are expected to provide the most

²⁸ The metrics have been presented at the LSST Project and Community Workshop 2021 in Survey Strategy III: Domain-Specific Cadence Optimization Discussions (project.lsst.org/meetings/rubin2021/content/survey-strategy-iii-domain-specific-cadence-optimization-discussions). A joint session of the AGN, TVS microlensing, and Strong Lensing scientific collaborations titled ‘Together we Stand!’ was held during the second SCOC science collaboration workshop (<https://project.lsst.org/meetings/scoc-sc-workshop2/agenda>).

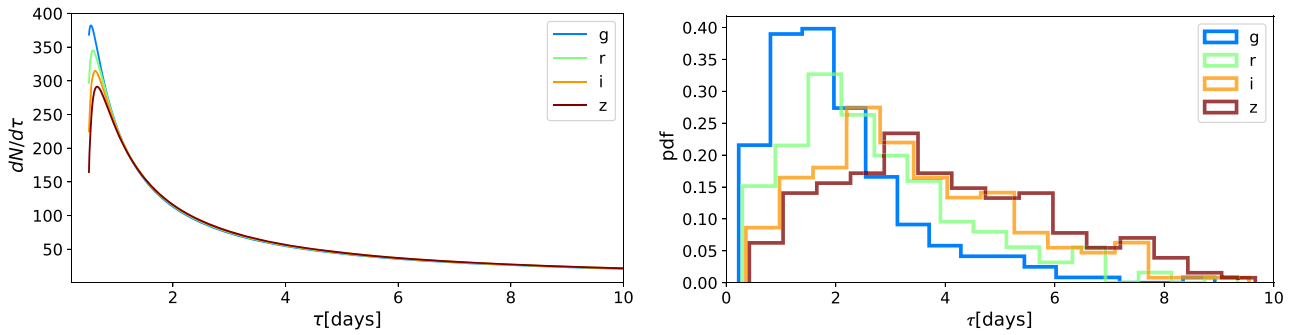


Figure 1. Left: distribution of quasars per expected time lag with respect to the u -band filter based on an ideal set of uniform distributed masses in the range 10^6 – $10^{10}M_{\odot}$. Right: PDF of expected time lag with respect to the u band for the 208 quasars sample from Liu et al. (2019) and Shen et al. (2011) catalogs located in COSMOS.

complete catalogs of AGNs and their host galaxies (Brandt et al. 2018; Zou et al. 2022).

We used our metric (Kovačević et al. 2021b) simulation in the LSST MAF to test various cadence strategies. For the best strategies revealed by our metric MAF simulations, we simulated AGN light curves using a damped random walk (DRW) model, as the simplest Gaussian random process model that can describe the optical light curves of quasars more-or-less reasonably well (Kelly et al. 2009; Kozłowski et al. 2010; Zu et al. 2013). However, the following limitation of the DRW model should be kept in mind: as Kozłowski (2017) identified, it is important that the time baseline of the light curve is considerably longer than the damping timescale. Also, Stone et al. (2022) implied that even a 20 yr baseline is unlikely to be long enough to constrain the damping timescale in some of the quasars in their sample. This could be due to long-term trends in the light curve, or that these processes are more complex than a basic DRW with only one characteristic timescale (see Stone et al. 2022). We also used the AGN lamppost²⁹ AD model (Cackett et al. 2007) to account for wavelength dependence and replicate delayed LSST multiband light curves. Following that, we used OpSim 1.7–2.0 to produce data points for the delayed multiband light curves based on observational sequences of different cadences. We used a shifting method inspired by PyCS (Tewes et al. 2013) but with partial curve mapping (PCM; Jekel et al. 2019) to determine the similarity of shifted curves in order to calculate the time delay from the simulated observations.

The following is a general outline of the structure of the article. Section 2 answers the question of what lags are expected for different black hole masses. Section 3 describes the assumed accretion disk model, and how the synthetic light curves, which are used to probe the optimal cadences indicated by our metric, are constructed. Section 4 describes two tiers of estimators of cadence strategies. The first tier shows our metric run, which quantifies the optimal LSST cadences for AD time lag measurements using the LSST MAF. In the second, LSST multiband light curves are created under the assumption of generic quasar parameters and optimal LSST cadences, and their time delays are assessed with respect to the u band. Section 5 presents the results, which are interpreted and discussed in Section 6 in more detail. Section 7 concludes the article and presents further implications of this work.

²⁹ The lamppost is typically considered a pointlike source hovering over the black hole spin axis and associated with the X-ray corona.

2. Distribution in Time Lag of LSST Observable AGNs

For RM, it is not only interesting to know the efficiency of the survey observing strategies, but also which lags are expected for different black hole masses. For this purpose, we use the quasar luminosity function (QLF; Hopkins et al. 2007) to derive a probability density of AGNs per measured time lag. The probability for measuring the time lags $p_{\tau} = p(M, L, z)$ is estimated from a uniform sample of SMBH masses $M \in (10^6, 10^{10})M_{\odot}$, whose luminosities are inferred according to the procedure described in Kovačević et al. (2021b) and use the standard thin-disk model to calculate the expected mean time lags corresponding to LSST filters. The probability p_{τ} in our approach equals to our metric (containing expected mean time lags with respect to the u band) divided by the total number of measurements. The distribution in time lag (τ) of LSST observable AGNs is given by:

$$\frac{dN}{d\tau} = 4\pi \frac{d^2V}{d\tau dz} \int_{\log L(z)}^{+\infty} \frac{d^2\mathcal{N}}{d \log L dV} p_{\tau} d \log L dz \quad (1)$$

where $\frac{d^2\mathcal{N}}{d \log L dV}$ is a double-power-law QLF with redshift-dependent slopes from Shen et al. (2020; see their Table 4, second column) and $\frac{dV}{dz}$ is the comoving volume per redshift (calculated with CosmoLoPy³⁰).

Based on this, we summarize the expected distribution in time lag of LSST-observable AGNs in Figure 1 (left). In addition to this general distribution, as a forecast for the distribution of the observed time lags in LSST DDFs, we built a sample of 208 broad-line AGNs located within the COSMOS field, with estimated optical spectral parameters from the SDSS DR7 catalogs of Liu et al. (2019) and Shen et al. (2011). If an object is identified in both catalogs, we used the data from Liu et al. (2019) as it provides the most up-to-date measurements of the AGN spectral parameters. The resulting sample covers a large range of redshifts ($z = 0.02$ – 3.82) and black hole masses ($\log(M/M_{\odot}) = 6.6$ – 10.3). As in the case of an ideal uniform set of SMBH masses, we use the standard thin-disk model to calculate the expected time lags in LSST $ugriz$ bands. The right panel of Figure 1 shows the probability density function (PDF) of the predicted time lag. Both distributions show that a majority of AGNs will have lags less than 5 days. We can expect that higher observational cadences, such as `multi_short`, may increase the rate of detected time lags. As the LSST will provide higher-resolution images and multivisit

³⁰ <http://roban.github.com/CosmoLoPy/>

multiband data sets, our estimate is most likely a lower threshold.

3. Synthetic Light Curves for Probing LSST Optimal Cadences

Here, we outline the calculation of synthetic time-delayed AD light curves using a combination of a theoretical AD transfer function (Section 3.1) and a DRW (Section 3.2).

3.1. Accretion Disk Model and Expected Time Lag

We assume a nonrelativistic thin-disk model (Shakura & Sunyaev 1973) that emits blackbody radiation and has a compact variable source (a “lampost”), whose photons hit the disk and cause a local temperature increase; full details can be found in the literature (Cackett et al. 2007; Pozo Nuñez et al. 2015; Starkey et al. 2016, 2017). Here, we summarize the key points. We assume an optically thick and geometrically thin accretion disk. The total observed energy flux Ξ from the accretion disk is a sum of the energy flux radiated due to a viscous heating process Ξ_V from a surface unit and irradiated flux Ξ_I of the disk photosphere, $\Xi = \Xi_V + \Xi_I$ (Pozo Nuñez et al. 2019).

If R is the radial distance from the disk’s innermost radius, $R_0 = \frac{6GM}{c^2}$ for a nonspinning SMBH, G is the gravitational constant, M is the SMBH’s mass, and \dot{M} is the mass accretion rate, then

$$\Xi_V = \frac{3GMM\dot{M}}{8\pi R^3} \left(1 - \sqrt{\frac{R_0}{R}}\right).$$

Because the geometry of the emitting source is unknown in the lampost model, a crude approximation is established by setting the source of luminosity L^* ³¹ at a height h^* along the SMBH’s rotational axis. Then the irradiative flux might be calculated using the disk’s albedo A as follows (Pozo Nuñez et al. 2019):

$$\Xi_I = \frac{L^*(1-A)}{4\pi R^3} h^* \cos \theta$$

so that θ is the incident angle between the disk surface normal and radiation of the emitting source (Netzer 2013). For viscous heating alone, when $R \gg R_0$ the disk temperature profile should follow

$$T(R) = \left(\frac{3GMM\dot{M}}{8\pi R^3 \sigma_{\text{SB}}}\right)^{1/4}$$

where σ_{SB} is the Stefan–Boltzmann constant. Similarly, in the case of irradiation of the disk from a height h^* above the disk, the total temperature profile is a superposition of the temperature due to irradiation and the temperature due to viscous heating

$$T^4(R) = \left(\frac{3GMM\dot{M}}{8\pi R^3 \sigma_{\text{SB}}}\right) + \frac{L^*(1-A)}{4\pi R^3 \sigma_{\text{SB}}} h^* \cos \theta.$$

That is,

$$T(R) \propto \left(\frac{L^* h^*}{R^3}\right)^{1/4}$$

for $R \gg h^*$ and the viscous heating flux is much smaller than the irradiated flux (Pozo Nuñez et al. 2019). Thus, in both cases, we expect that the temperature profile follows the relation $T(R) \propto R^{-3/4}$ (Cackett et al. 2007). We assume that reprocessing has a minor effect on deviations from the viscous temperature and the $T(R) \propto R^{-3/4}$ temperature structure (see Collier et al. 1998; Starkey et al. 2016):

$$T(R) = \left(\frac{3GMM\dot{M}}{8\pi \sigma_{\text{SB}} R_\lambda^3}\right)^{1/4} \left(\frac{R_\lambda}{R}\right)^{3/4} \sim \left(\frac{3GM^2 L}{8\pi \eta c^2 L_{\text{Edd}} \sigma_{\text{SB}} R_\lambda^3}\right)^{1/4} \left(\frac{R_\lambda}{R}\right)^{3/4}. \quad (2)$$

Here, L_{Edd} is the Eddington luminosity ($L_{\text{Edd}} \approx 1.3 \times 10^{38} \frac{M}{M_\odot} \text{erg s}^{-1}$), η is the accretion efficiency. If we are observing at rest wavelength λ^{rest} , the radius R_λ is usually approximated as the radius where the disk temperature matches the photon wavelength

$$kT = \frac{hc}{\lambda^{\text{rest}}};$$

here, h and k are the Planck and Boltzmann constants, respectively. Then the radius corresponding to the photon wavelength of LSST filters is

$$R_\lambda \sim \left(\frac{k\lambda}{hc}\right)^{4/3} \left(\frac{3GMM\dot{M}}{8\pi \sigma_{\text{SB}}}\right)^{1/3} \sim \left(\frac{k\lambda}{hc}\right)^{4/3} \left(\frac{3GM^2 L}{8\pi \eta c^2 L_{\text{Edd}} \sigma_{\text{SB}}}\right)^{1/3}. \quad (3)$$

The disk transfer function $\psi(\tau, \lambda)$ describes the response of the disk to changes at a given wavelength and time delay (Cackett et al. 2007):

$$\psi(\tau, \lambda) = \int_{R_{\text{in}}}^{R_{\text{out}}} \int_0^{2\pi} \frac{\partial B}{\partial T} \frac{\partial T}{\partial L} \frac{R dR d\theta \cos i}{D^2} \times \delta\left(\tau - \frac{R}{c}(1 + \sin i \cos \theta)\right) \quad (4)$$

where L is the driving luminosity, i is the inclination angle of the disk, θ is the azimuthal angle of emission patch, D is the distance of the object, and $(R_{\text{in}}, R_{\text{out}})$ are inner and outer boundary of integration (see Cackett et al. 2007, and references therein). Also, we assume the accretion disk flux arises from the blackbody radiation described by Planck’s law

$$B(T) = \frac{2hc}{\lambda^5} \frac{1}{e^{\frac{hc}{\lambda kT}} - 1}$$

with the temperature profile given by Equation (2).

If we assume the temperature variations to be small, then the derivative is

$$\left| \frac{\partial B}{\partial T} \frac{\partial T}{\partial L} \right| \sim \frac{q \cdot x^{-1/4} e^{qx^{3/4}}}{4(e^{qx^{3/4}} - 1)^2},$$

³¹ Vasudevan et al. (2009) estimated that about 5% of total flux comes from an X-ray source.

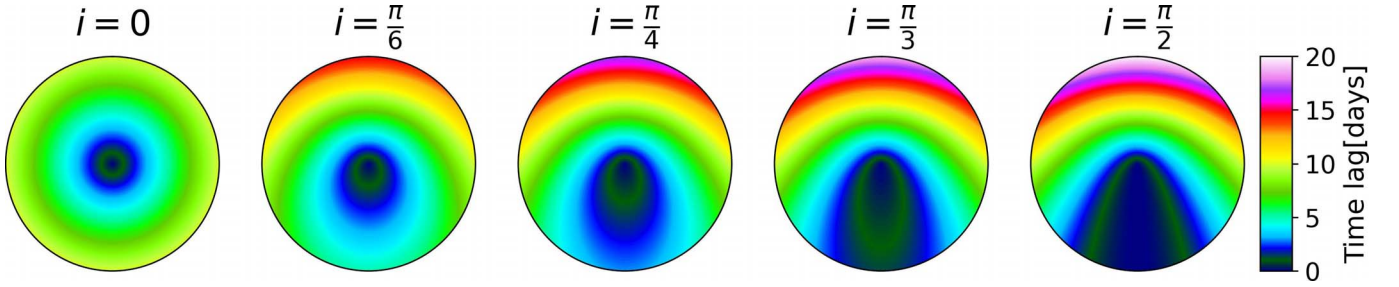


Figure 2. Flat accretion disk time delay distributions ($\tau(r, \theta, i) = r(1 + \cos \theta \sin i)/c$), as seen by a distant observer, for various inclinations i given on top of each plot. The theoretical observer position is to the bottom at infinity. The color bar (in units of days) indicates time lag values. Distributions are deformed from circular to elliptical and becomes parabolic for the extreme inclination $i = \pi/2$. The observer will witness the re-emitted light arriving with delays ranging from 0 to $2r(1 + \cos \theta \sin i)/c$, with a bulk average delay of $r(1 + \cos \theta \sin i)/c$ for radius r and azimuth θ of the reprocessing site, with $r \in [0, 10]$ lt-days. Our disk model reiterates the concept of isodelay surfaces as described in Peterson (2006) and Starkey et al. (2016).

where $x = \frac{R}{R_\lambda}$, $q = hc/\lambda k$.

For our blackbody disk model, the time-delay centroid $\langle \tau \rangle$ of the transfer function is³²

$$\langle \tau \rangle = \frac{\int \psi(\tau, \lambda) \tau d\tau}{\int \psi(\tau, \lambda) d\tau} \sim \frac{\int \psi(\tau, \lambda) \frac{R^2}{c} dR}{\int \psi(\tau, \lambda) R dR}. \quad (5)$$

Figure 2 illustrates the differentiation of the time lag distributions within the disk with regard to different inclinations. Each region of distribution is labeled with the time delay it represents (so that we would observe relative to the continuum source). This is a well-known notion of isodelay surfaces, as described in Peterson (2006) and Starkey et al. (2016). The line of sight to the observer is oriented toward the bottom of each disk plot, except in the left panel, where it is exactly vertical to the plot plane.

Also, we plot example response functions showing the LSST wavelength dependence in Figure 3 for the following set of parameters: SMBH mass $M = 2 \cdot 10^8 M_\odot$, $L/L_{\text{Edd}} \sim 0.1$, $\eta = 0.1$, disk inclination of 45° , and azimuth angle of 0° . As shown in Figure 3, the mean delay, indicated by the vertical lines, and the width of the response functions increase with wavelength. These effects occur due to the inverse scaling between temperature and radius (Starkey et al. 2016).

In addition, a larger inclination of the disk (see Figure 2) makes the response function more skewed (Starkey et al. 2016). The peaks will move toward shorter lags and develop a tail toward large lags. This occurs because larger inclinations increase the lag on the far side and shorten the lag of the near side (Starkey et al. 2016) relative to smaller inclination (see Figure 2). A simple sinusoidal with a period of 2.5 days was constructed to demonstrate how its peak positions and amplitudes change while convolving with the time-delay transfer function of a disk with an inclination of $\pi/4$ and for different LSST filters (see Figure 3).

Figure 4 demonstrates potential effects of a nonrelativistic AD setup by comparing the observed luminosity normalized to the accretion rate for classical and Kerr-metric blackbody disk emission as given by the Campitiello et al. (2018); see their

³² Taking into account that the integral $I(a) \sim \int_{(a^2-1)^2}^{a^2} ds$ can be evaluated numerically (Cackett et al. 2007), and that the centroid time delay can be approximated as follows:

$$\langle \tau \rangle \sim \frac{R_\lambda (\lambda k)^{4/3} I(8/3)}{c (hc) I(4/3)}$$

where $I(8/3) = 5.139$, $I(4/3) = 2.895$.

Figure 2) as a function of SMBH spin a and viewing angle θ . It is easy to notice that for $a < 0.8$, the relativistic angular pattern of radiation is very similar to the classical behavior. The classical model, when observed at $\theta = 0$ is well approximated by the relativistic model with $a \sim 0.8$, but at larger viewing angles, the relativistic model is brighter because of the strong relativistic effects. When spin $a \rightarrow 1$, the radiation pattern is very steep, even for the largest viewing angles. This is due to the combination of different relativistic effects (Doppler beaming, gravitational redshift, and light bending) along with the black hole spin: the trajectories of the energetic photons coming from the innermost region of the disk (close to the event horizon) are bent in all directions, and the intensity of radiation is almost the same at all viewing angles.

To compare time lags in curved and flat spacetime, we calculate their ratio. Time lags in curved space are obtained by combining analytical approximation of time delay for a Kerr black hole in flat spacetime (e.g., Campana & Stella 1995; Mastroserio et al. 2018) and approximation for light bending (Poutanen & Beloborodov 2006):

$$c\Delta t = ry \cdot \left(1 + \frac{uy}{8} + \frac{uy^2}{8} \left(\frac{1}{3} - \frac{u}{14} \right) \right) \quad (6)$$

where r and θ are radius and azimuth of reprocessing site, $u = \frac{2GM}{c^2 r}$, and $y = 1 + \cos(\theta) \sin(i)$ for a given inclination i . Note that $c\Delta t = ry$ corresponds to the time delay one would expect in flat spacetime (see Figure 4).

Figure 5 depicts a schematic view of the 2D distribution of the ratio between the relativistic time delay (Equation (6)) and its classical equivalent. The ratio values are sharply increasing with decrease of distance to the center of mass. This is due to light bending, which is largest there. For a nonrotating black hole ($a \rightarrow 0$), the marginally stable radius is $r_{\text{ms}} = 6 \frac{GM}{c^2} = 6r_g$, while for a maximally rotating black hole ($a \rightarrow 1$), it takes a value of $r_{\text{ms}} = 1 \frac{GM}{c^2} = r_g$. As theoretical predictions state that the maximal spin for a rotating black hole cannot exceed 0.998, then the marginally stable radius of fast-rotating black hole is $r_{\text{ms}} = 1.24r_g$ (Thorne 1974). Figure 5 corresponds to fast-rotating $a \rightarrow 1$ SMBH, so that the small white inner circle with radius of the marginally stable orbit $r_{\text{ms}} = 1.24r_g$ assumes that no source of light can orbit around SMBH. As for nonrotating $a \rightarrow 0$ SMBH, at $6r_g$ and larger distances there will be no effects (dark green and dark blue color). The upper limit of the navy blue region is at $6r_g$. Therefore, for a fast-rotating SMBH, relativistic corrections should be taken into account, because r_{ms} is closer to the event horizon. Even though it looks like an extreme possibility, there are well-known cases like

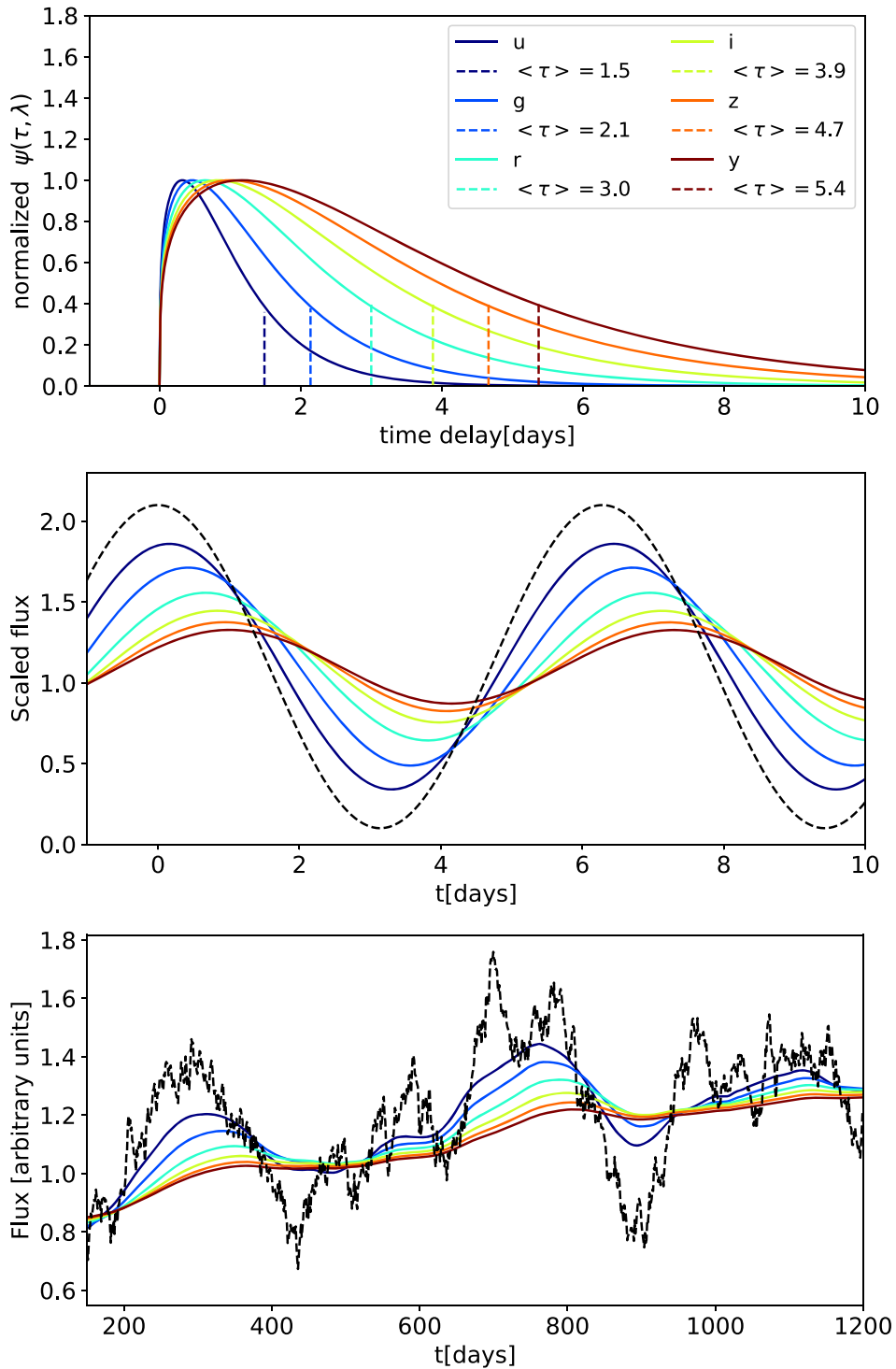


Figure 3. Top: numerical accretion disk transfer function for LSST *ugrizy* filters calculated for the following set of parameters: SMBH mass $M = 2 \cdot 10^8 M_\odot$, $L/L_{\text{Edd}} \sim 0.1$, $\eta = 0.1$, disk inclination of 45° , and azimuth angle of 0° . Dashed vertical lines mark the theoretical centroid delay (Equation (5)) for comparison with the peaks for each transfer function (values given in the upper-right corner). Middle: convolution (in colors) of transfer function and a sinusoid of 2.5 days period (shown in dashed black). Bottom: synthetic LSST light curves obtained by convolution of the driving light curve, the flux of which is scaled (black line) and inclined AD transfer function shown in top panel. Different bands are plotted with the same color coding in all plots.

MCG-6-30-15 and NGC 4051, whose X-ray emission could be explained with light-bending effects (e.g., Dai et al. 2010; Chartas et al. 2012; Kara et al. 2014). Also, the published EHT observations of M87 and Sgr A* are consistent with the Kerr paradigm, indicating that fast spinning black holes might be ubiquitous cases (Event Horizon Telescope Collaboration et al. 2019, 2022).

3.2. Simulating Driving and Multiband Light Curves

We provide here a summary of our light-curve modeling. A full description of synthetic light-curve modeling, and of tests using these synthetic light curves, is presented by Kovačević et al. (2021b).

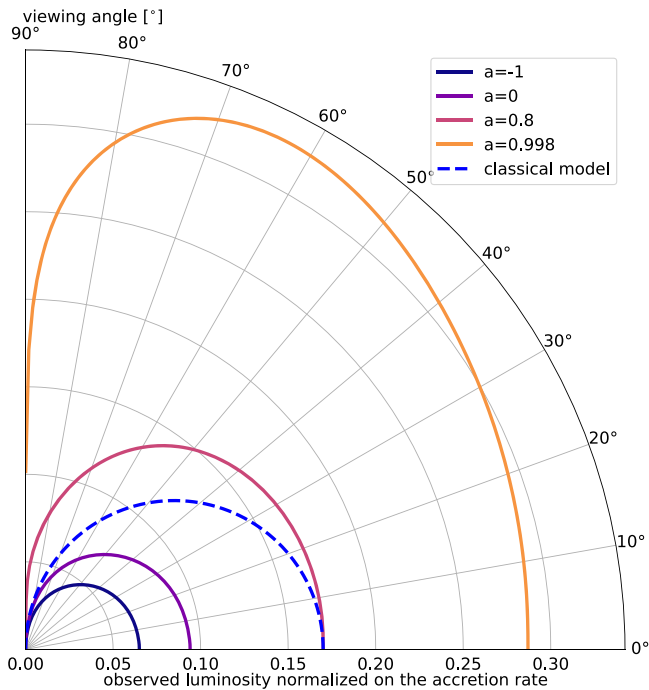


Figure 4. Schematic comparison of emission patterns across viewing angles for different AD models as given by the phenomenological approximation of Campitiello et al. (2018; see their Figure 2). The classical nonrelativistic model (dashed blue line) is compared with relativistic models with $a = -1$ (dark blue curve), $a = 0$ (dark purple curve), $a \sim 0.8$ (red curve), and $a = 0.998$ (orange curve). The radial axis is the observed efficiency $\eta_o = \frac{L_o}{\dot{M}c^2}$, i.e., given by the observed luminosity normalized on the accretion rate (which is the same for each model). The plot plane is the accretion disk plane. The main axis of all models is in the direction of 0° , assuming azimuthal symmetry with respect to this direction. A distant observer is at the left of the figure.

The time variability of AGN and quasar continuum emission can be approximated using a DRW (Kelly et al. 2009; Kozłowski et al. 2010; Zu et al. 2013). A DRW is defined by a stochastic differential equation with a broken power-law power spectrum and a slope that steepens from 0 to 2 above a break timescale. The break timescale in AGNs measured with the SDSS is up to 100 days. It correlates favorably with black hole mass and wavelength, and is a weak function of brightness (MacLeod et al. 2010; Burke et al. 2021). However, light curves of AGNs observed with Kepler and ground-based surveys show steeper power spectral density than the DRW model at timescales up to ~ 1 month (Mushotzky et al. 2011; Caplar et al. 2017; Smith et al. 2018; Sánchez-Sáez et al. 2018). Kozłowski (2017) demonstrated that light curves with insufficient time length cannot consistently constrain the damped variability timescale, and advised that light curve’s time length should be at least tenfold that of the true damped variability timescale. Based on 1384 variable AGNs from the QUEST-La Silla AGN variability survey, Sánchez-Sáez et al. (2018) showed that the DRW variability amplitude is influenced by the length of the light curve, and that the DRW model can represent the variability of 74% of AGNs in their specified sample. On the other hand, the work of Lu et al. (2019) suggests that only 35% of light curves in their RM AGN sample of 113 objects can be derived with accurate DRW model parameters. This proportion is much lower than that found by Sánchez-Sáez et al. (2018), which could be related to the RM AGN shorter light-curve length (1 yr) in Lu et al. (2019) than for the sample of Sánchez-Sáez et al. (2018). In this work, the probed damped variability timescales are short, up to 200 days with respect to LSST’s 10 yr time baseline, so that we

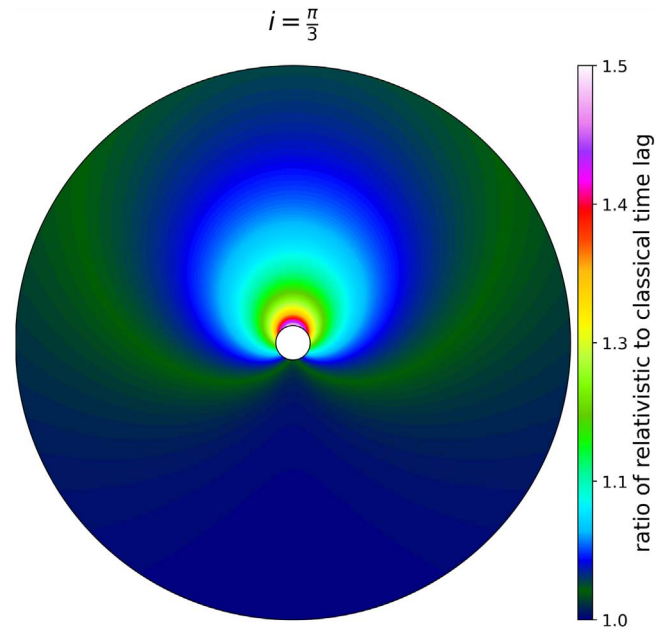


Figure 5. Distribution of ratio of the time delay calculated from a relativistic and a classical spacetime approximation, when $a \rightarrow 1$. The inclination of the observer is set to $i = \frac{\pi}{3}$, the region extent to $10r_g$, and the SMBH mass is $10^8 M_\odot$. The dark green color depicts a ratio value of ~ 1.075 . The small white circle is a ‘plunging region’ inside the marginally stable orbit of $r_{ms} = 1.24r_g$. The color bar shows the ratio between relativistic and classical time lags. The ratio is highest where the light-bending effects are largest, i.e., near the SMBH. As the distance increases, the ratio approaches 1, because spacetime is almost flat.

can assume that DRW is an approximate working description of quasar variability for optical light curves (Suberlak et al. 2021). Although the damping mechanism is unknown yet, Kelly et al. (2009) showed that the damping timescale might be connected to the thermal timescale of the accretion disk, assuming that its thermal fluctuations are responsible for the AGN variability. Because of this, we concentrate our analysis on the DRW model, based on its implementation in Zu et al. (2011, 2013) and Suberlak et al. (2021).

Neustadt & Kochanek (2022) investigated the effect of AD temperature fluctuations on AGN light curves, revealing that the light curves closely reflect the expectations for a lampost model, albeit with slower variability timescales of the ingoing waves. This also means that longer timescale variability signals will increasingly diverge from conventional models, since the smoothing of slower-moving waves reduces significantly as their period or spatial wavelength grows. LSST will operate much longer than most RM campaigns, providing the first well-characterized multiwavelength light curves to investigate what happens on long timescales.

We first generate a uniform time grid $\Delta t_i = 1$ day on which to evaluate the driving light curves F_{DRW} . This is convenient for evaluating the convolution integral. As the AD transfer function’s asymmetry increases with an increase in the wavelengths of the filters, light-curve features are still evident in the u band for the shortest wavelength, but they are blurred out for the y band (see Figure 3 and Section 6). Since the y -band light-curve distortion is the greatest, determining the time lag requires additional care (due to large possible errors). Thus, for the sake of simplicity, we continue by generating quintets of multiband light curves based on the LSST $ugriz$ bands using a transfer function as described in Section 3.1.

The multiband continuum light curves ($\mathcal{F}(t, \lambda)$) are then obtained from the driver (F_{DRW}) by convolution with the asymmetric response function $\psi_{\lambda}(\tau)$ (see an example in Figure 3):

$$\mathcal{F}(t, \lambda) = \sum_{i=0}^m \psi(\tau_i, \lambda) F_{\text{DRW}}(t - \tau_i) \Delta\tau. \quad (7)$$

We assume the following set of parameters for the transfer function: SMBH mass $M = 2 \cdot 10^8 M_{\odot}$, $L/L_{\text{Edd}} \sim 0.1$, $\eta = 0.1$, disk inclination of 45° , and azimuth angle of 0° . For the driving source emission, we assume a characteristic rest-frame timescale $\tau_{\text{DRW}} \sim 200$ days and a structure function at infinity $\sigma_{\text{DRW}} = 2.5$ (flux unit), which describes the long-term variability of the light curve. These DRW parameters are typical of the quasars in the DES sample (Yu et al. 2020). In general, MacLeod et al. (2010) found that both parameters follow a power-law relationship with AGN luminosity, measured wavelength, and black hole mass (see King et al. 2015, for a compact representation of these relations).

A realization of the driving source emission for given parameters is displayed in the bottom panel of Figure 3 in black. Using the transfer functions for the LSST bands, we then generated the multiband light curves³³ as shown in the bottom panel of Figure 3. In practice, light curves where the lags are not clearly visible are likely to have delays that are shorter than the cadence of the light curve.

4. Estimator of Cadence Strategies

In this section, we characterize distinct LSST observing strategies. Section 4.1 describes our metric implemented in MAF that quantifies the impact of cadences for LSST RM time lag measurements. Additional calculations of time lag measurement of simulated LSST continuum light curves using the best cadences identified by our metric in two DDFs are outlined in Section 4.2.

4.1. Metric Simulation in MAF

MAF³⁴ is a software package designed to enable writing code to evaluate the performance of different survey strategies. Our metric is integrated into MAF through the module `AGN_TimeLagMetric`³⁵.

The metric includes the quasar selection based on the limiting magnitude of the observation³⁶ in the r filter. The magnitudes were corrected for the Galactic dust extinction. The sky regions with dust extinction $E(B - V) > 0.2$ are excluded because this amount of dust extinction is problematic for extragalactic science for two reasons: it reduces the effective coadded 5σ depth³⁷, and the total amount and wavelength dependence of dust extinction are not always well characterized, making it difficult to calibrate the effect on the background galaxies (see Jones et al. 2020).

The depth of LSST single visits is assumed to be similar to that of the COSMOS field observations by the VLT Survey Telescope (De Cicco et al. 2021). De Cicco et al. (2021) found that 91% of AGNs

have $r > 21$ mag, putting them beyond the average depth of most existing variability studies. Thus we impose in our MAF simulations a cut for 5σ depth in the r band > 21.0 mag.³⁸ This enables us to investigate how well AGN time lag measurements work for fainter objects. Our later analysis reveals that the most suitable DDF cadence strategies in the r band have mean 5σ depths of 21.5 (see discussion in Section 6, and Figures 11–13). Application of our metric with concurrent limitations in all filters could eliminate the vast majority of visits for time lags up to 5 days due to the Nyquist criterion. Otherwise, for larger time delays (of the order of tens of days), simultaneous 5σ cuts can be used in more than one band. Thus, we relaxed the limitation in bands other than r in order to have a broader pool of feasible cadences in the other bands. When we compared the mean 5σ depths of r and other bands within the DDFs, we found that they are within the range of 18 and 21.5 mag in DDFs (Figures 11–13). This means that objects as bright as 21 mag will still be seen in those bands for these overlapping cadence strategies.

When analyzing observations of variable objects, two major issues arise. First, because of weather or other technical constraints, sampling times can be perturbed. Second, objects can have a wide range of variability characteristics and behaviors. As a result, it is important to establish a threshold to search for variability on the timescales of interest (Eyer & Bartholdi 1999). By assuming that there is no correlation between flux variation F_{var} (as defined in, e.g., O’Brien et al. 1998), the measured time delay τ_{obs} , and its uncertainty $\sigma_{\tau_{\text{obs}}}$, Kovačević et al. (2021b) developed the metric ϕ_{τ} :

$$\log \phi_{\tau} = \log \frac{\sigma_{\tau_{\text{obs}}}}{\tau_{\text{obs}}} \propto A + C_1 \frac{F_{\text{var}}}{\sigma} + C_2 \frac{\tau_{\text{obs}}}{(1+z)\Delta t^c}, \quad (8)$$

where the time sampling (or cadence) of the light curve is Δt^c , and the mean photometric error of the light-curve points is σ . If the observed variation is intrinsic to the quasars at cosmological distances, one would expect a time dilation effect. The time delay is reduced to the rest frame, taking into account the cosmological redshift z in Equation (8) by a factor $(1+z)^{-1}$.

As the expected size of the AD in the UV/optical is on the order of $\lesssim 10$ lt-days where the Nyquist criterion becomes important, we modify our metric³⁹ as follows:

$$\log \phi_{\tau} \propto \frac{\tau_{\text{obs}}}{(1+z)\Delta t^c}. \quad (9)$$

Note that the fraction term on the right-hand side of Equation (9) represents a sampling rate. There are different opinions in the literature when it comes to the sampling rate (Δt^c) for irregularly sampled data. Some authors (e.g., Horne & Baliunas 1986; Press et al. 1992) associate the Nyquist frequency with $1/2\langle t_{\text{sam}} \rangle$, where $\langle t_{\text{sam}} \rangle$ is the averaged sample rate, or with $1/(2s)$, where s is the smallest time sampling in the sample (Scargle 1982; Roberts et al. 1987).

For irregular sampling, Eyer & Bartholdi (1999) defined the Nyquist frequency as $f_{\text{Ny}} = 1/(2p) > 1/(2s)$, where p is a

³³ In a work by Jankov et al. (2022), we determined which LSST filters contain a continuum at different redshifts (see, e.g., their Figure 1).

³⁴ https://rubin-sim.lsst.io/rs_maf/index.html

³⁵ https://rubin-sim.lsst.io/rs_maf/metricList.html

³⁶ The 5σ depth in the `OpSim` is the limiting magnitude of the visit—meaning, objects fainter than this limit will not be visible. However, objects brighter than that limit are definitely still visible, and at a signal-to-noise ratio greater than 5.

³⁷ The unit is magnitude, see <https://confluence.lsstcorp.org/display/SIM/Summary+Table+Column+Descriptions>.

³⁸ Otherwise, adding a cut for 5σ depth in the r band < 21.0 mag means that the (vast majority) of visits with depth > 21.0 mag would not be counted, yet could still detect objects that are as bright as 21.0 mag.

³⁹ The other terms could be kept less than an arbitrary constant, e.g., assuming limits of $F_{\text{var}} \sim 0.4$ and $\sigma \sim 0.005$ mag.

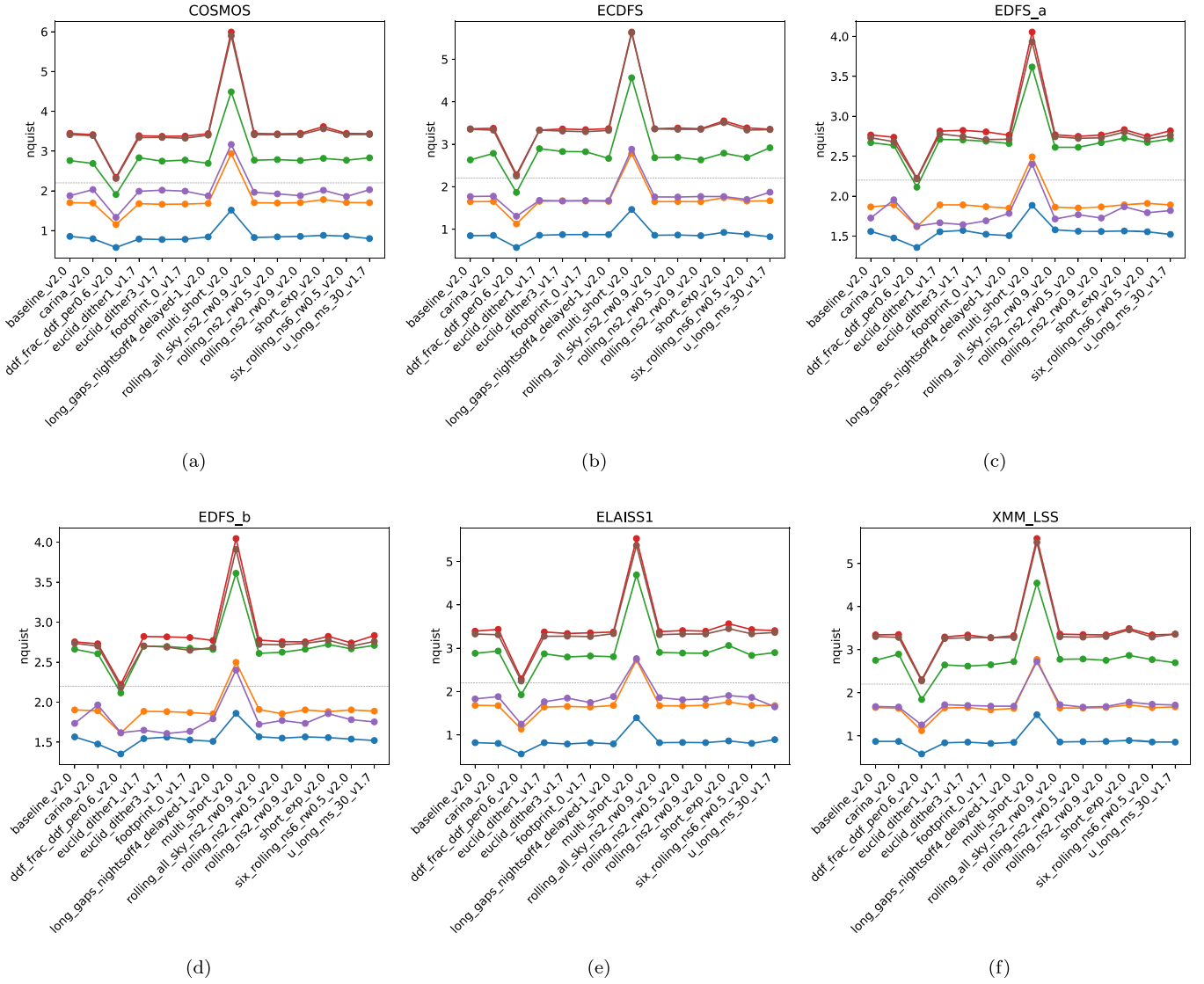


Figure 6. The comparison of metric values above the Nyquist threshold (y-axis) for the measurement of 5 day time lags in six DDFs, for various OpSim strategies indicated on the x-axis and six of the LSST filters stated in the legend. The solid lines serve as guides for the eye. The horizontal black line indicates the metric threshold. DDFs are indicated in the titles of panels. The passbands u , g , r , i , z , and y are denoted by blue, orange, green, red, violet, and brown, respectively.

greatest common divisor (gcd) for all $t_i - t_1$ of time of observation t_i . Since gcd calculation is very time consuming, we will use the definition based on the smallest cadence in the sample (Scargle 1982; Roberts et al. 1987).

It is critical that the light curves are sufficiently well sampled for RM. Recalling Nyquist’s Theorem, the sampling rate of the time lag measurement must be

$$\frac{\tau_{\text{obs}}}{(1+z)\Delta t^c} > 2.2$$

in order for the time lag to be evaluated (Haas et al. 2011). As a result, our metric evaluates whether the sampling rate for a required time lag measurement is greater than the Nyquist threshold.⁴⁰

⁴⁰ Due to data loss to weather or technical difficulties in reality, practical sampling might require a stiffer criterion, known as the engineer’s Nyquist (see, e.g., Srinivasan et al. 1998): $\frac{\tau_{\text{obs}}}{(1+z)\Delta t^c} > 2.5$.

4.2. Recovering Time Lags

For simulated quintets of AGN light curves in the LSST *ugriz* bands (Section 3.2), we estimate the time delay relative to the u band and compare it to the input value. We chose the u band as the reference band since its has the shortest wavelength. Moreover, as the cadence of u -band observations is a critical issue in the LSST observing strategy optimization (Brandt et al. 2018), we aim to probe if the u band can be used to evaluate AD time lags in the DDFs.

In addition to the standard cross-correlation methodologies for determining time lags (Gaskell & Sparke 1986; Gaskell & Peterson 1987; Alexander 1997), other methods have been developed as those built on the assumption of a DRW process (e.g., Zu et al. 2016), the DRW process combined with expansion of the transfer function into a series of Gaussian functions (Li et al. 2016), and shifting techniques (Tewes et al. 2013), to deal with complex light curves (Chan et al. 2020). For example, Kovačević et al. (2021a, 2021b) adapted the functionality of the widely used z-transformed discrete correlation function technique (Alexander 1997) to take into

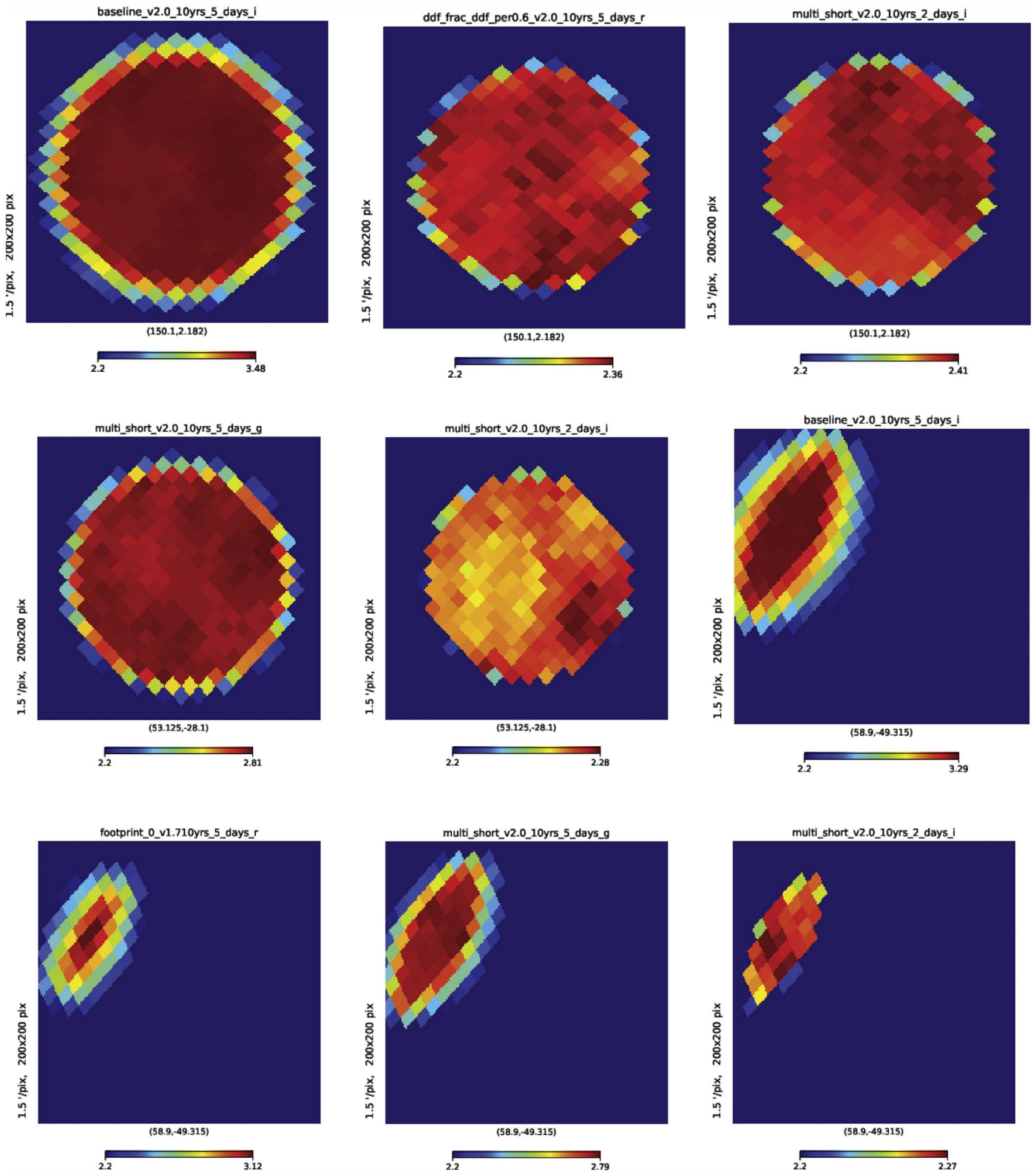


Figure 7. Zoom-in of metric values (indicated in color bars) in DDFs for different cadence strategies (given in panel titles) for the *r*, *g*, and *i* bands. Upper row: COSMOS. Middle row: first and second panels: ECDFS; third panel: EDFS_a. Bottom row: EDFS_a.

account general Gaussian processes in the modeling of the light curves. We employed our shifting method to estimate time delays from the mock data, which is inspired by the `PyCS` toolbox developed by Tewes et al. (2013). One of the `PyCS` implementations is optimized to find the best set of time delays

that minimizes the variability of the difference between Gaussian-process regressions on the light curves. This is motivated by the standard problem that there is a different number of light-curve data points. An alternative objective function is needed to measure the similarity between the

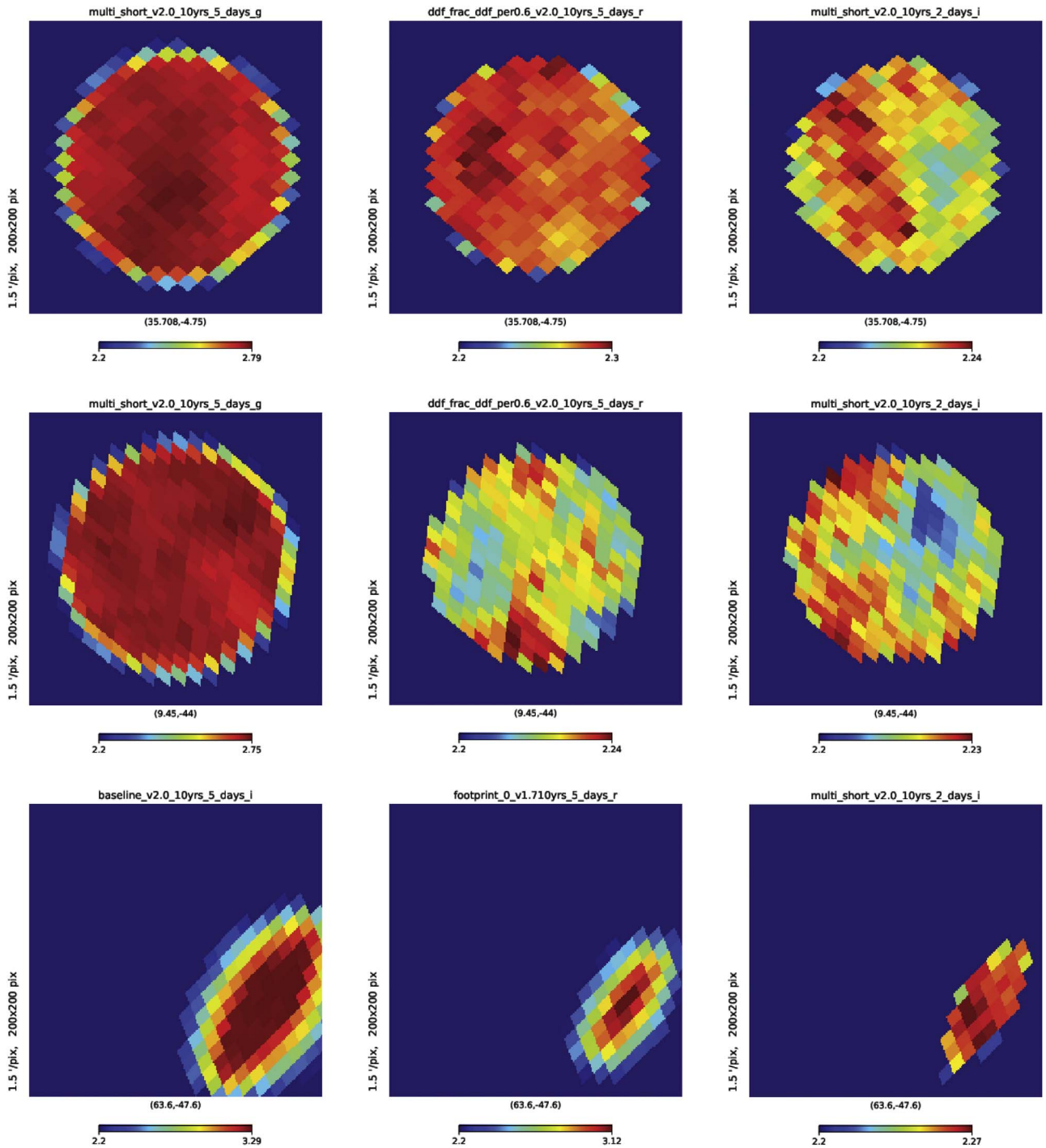


Figure 8. The same as Figure 7, but for XMM in the top row, ELAIS1 in the middle row, and EDFs_b in the bottom row.

curves. As multiband light curves are mainly deformed due to the asymmetric transfer function, our basic idea of the optimizer is to shift the data iteratively in time and magnitude with respect to a reference band, and apply the PCM⁴¹ (Jekel et al. 2019) method to determine the similarity between curves and estimate a time delay through minimization of the PCM.

For measuring the time lag τ between two noisy light curves, $f_1(t)$, $f_2(t)$, we fit the relation $f_1(t) = a \cdot f_2(t - \tau)$ where a is a scaling coefficient. Denoting the LSST light curves as $X = \{x_j(t_i) | i = 1, \dots, N, j \in (u, g, r, i, z)\}$, the scaling coefficients

and the lags as a_k and τ_k , $k \in g, r, i, z$, respectively, and finally the variances of the noise as v_k , we can fit the quartet of multiband light curves $\mathbf{x} = x_g, x_r, x_i, x_z$ with one predictor time series in the shortest wavelength x_u .

A prior estimate of the time delay range of light curves can be obtained through preprocessing with less precise algorithms (see, e.g., Tewes et al. 2013), available prior knowledge (see an example of R-L relation use in Penton et al. 2022), or expected ranges obtained from assumed AD model $L = \text{math.floor}(\langle \tau \rangle_k - \langle \tau_u \rangle)$, $k = g, r, i, z$ from AD model: $[L, L + 1]$. Considering the time lags that will be probed, we adopt the latter strategy, such that the uniform priors (in days) are:

⁴¹ https://github.com/cjekel/similarity_measures

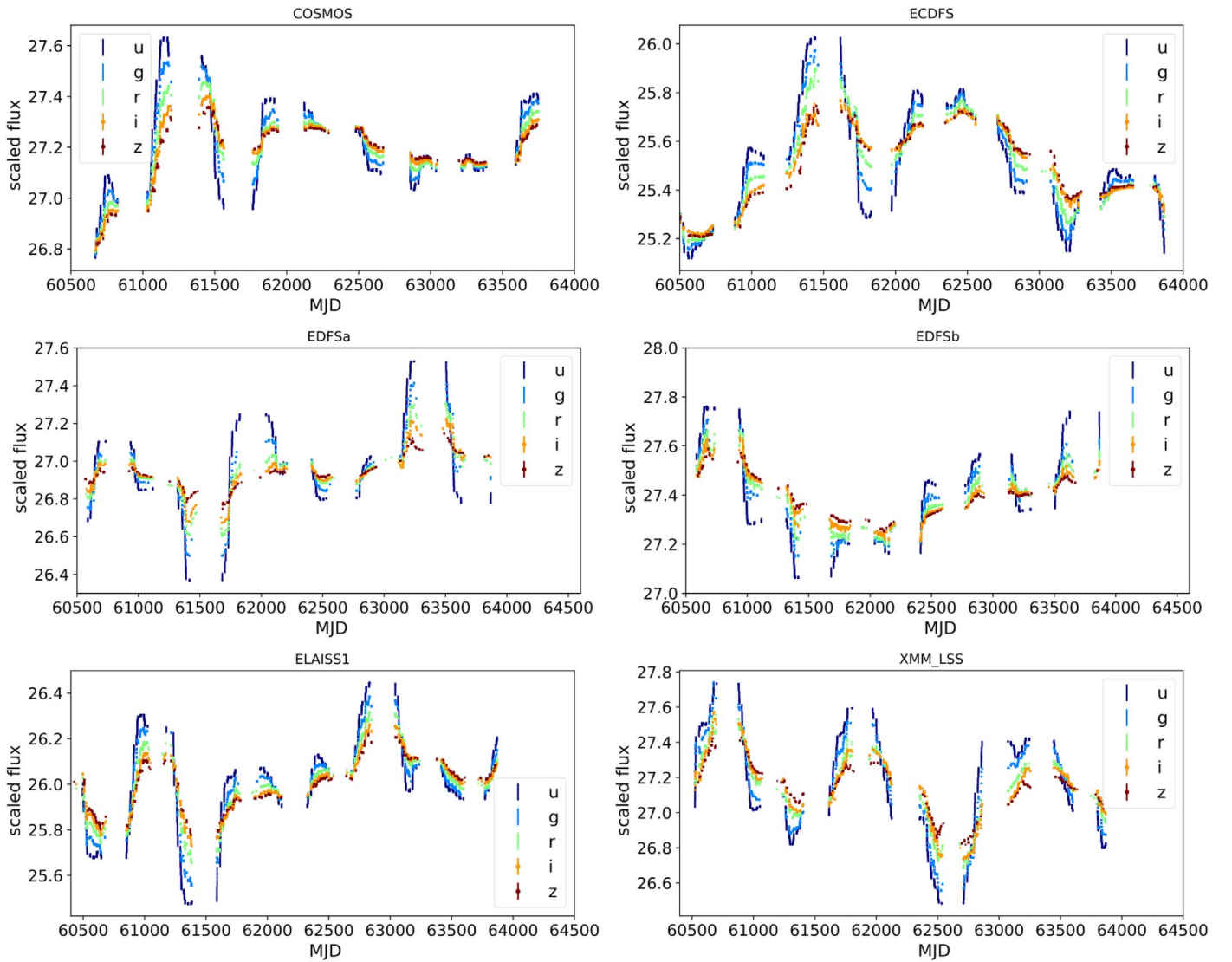


Figure 9. Examples of simulated quintets of LSST light curves for quasars in the LSST DDFs. We simulate the light curves over a period of 10 yr with `multi_short_v2.0_10yrs` cadences. The error bars are set at 0.005 mag rms.

$\tau_{ug} = \text{Uniform}(0, 1)$, $\tau_{ur} = \text{Uniform}(1, 2)$, $\tau_{ui} = \text{Uniform}(2, 3)$, and $\tau_{uz} = \text{Uniform}(3, 4)$. They reflect the range of expected values of difference between mean time delays of the transfer function in different bands. These should only be considered as suggestions, and can be easily changed. Priors on expected time lags are noninformative, and their ranges do not overlap. Our emphasis is on the fact that multiple models for the AD model and its transfer function could be used in a real-world setting, and that the prior on the time lag should reflect this. To determine the similarity of curves after scaling and shifting, we apply PCM, which combines arclength and area, because the choice of parameters can alter the overall length of the curve. We illustrate the principles of PCM, while details are given in Jekel et al. (2019). First, the arclength of the one curve is superimposed onto a section of the other curve. After that, trapezoids are created between the curves, and the areas of the trapezoids are added together. The best-fit PCM value is the one that minimizes the combined area of the trapezoids.

The PCM permits the use of nonresampled light curves; nevertheless, we followed the PyCS guideline and resampled them with a homogeneous cadence of ~ 0.5 –1 day. The time

lag and its uncertainty are calculated by fitting the resampled, shifted light curves to the u -band light curve using a random value drawn from the prior. The PCM space for each light curve is quite irregular, with multiple local minima. To discern the different minima objectively and without expectation bias, we repeat the procedure 300 times for each of the resampled light curves, using a sample of 100 random-uniform initial time lags. The most common time lag (corresponding to ‘dominant PCM minimum’) is regarded as the best-fitting value for the specific light-curve pair. Finally, from the distribution of fitted lag values, we compute PDFs, a mean time lag, and uncertainties as 16th and 84th quantile confidence intervals.

5. Results-cadence Strategies for AD Time Lag Measurement

We use the `OpSim_v2.0` and `OpSim_v1.7`⁴² cadence simulations. The annotation adopted here follows the LSST nomenclature for the simulations. For example, the label

⁴² https://github.com/lst/sims_featureScheduler

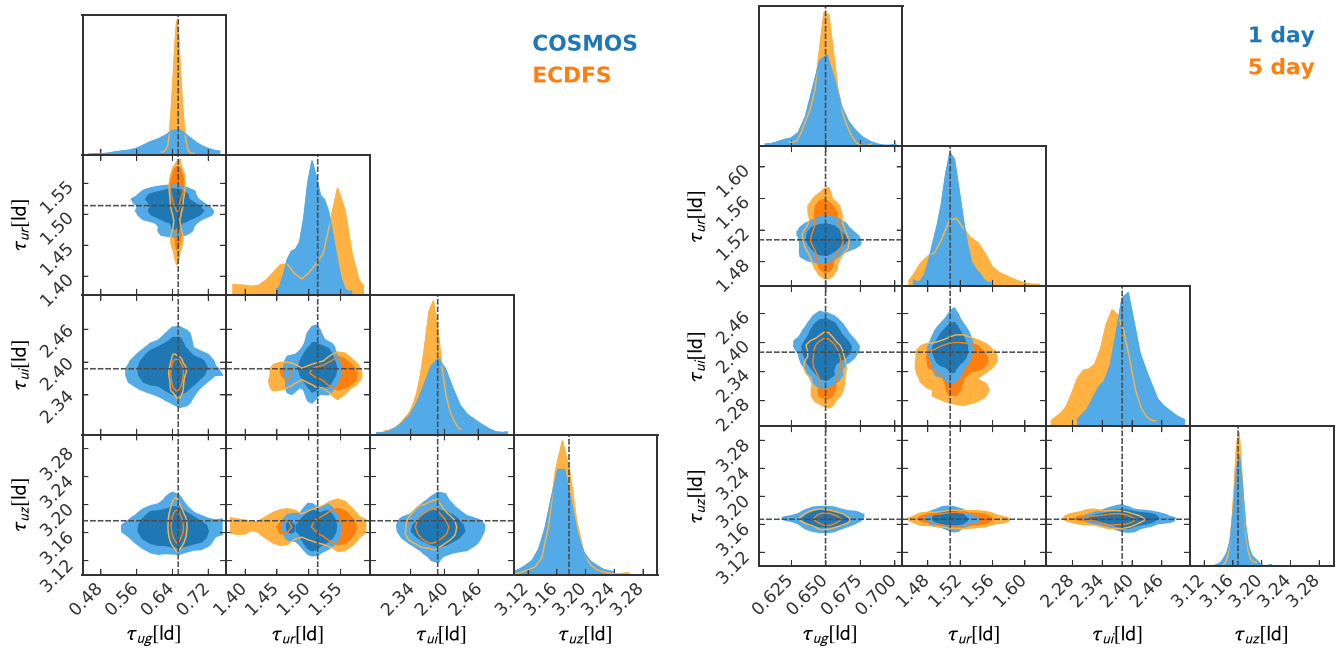


Figure 10. Corner plot showing the PDFs of the time lags of the synthetic light curves with DDFs COSMOS (blue) and ECDFS (orange) sampling (left) and homogeneous 1 day (blue) and 5 day (orange) sampling (right). The distribution for each time lag independently is shown in the histograms along the diagonal, and the 2D distributions are shown as contour plots in the other panels. The dashed black lines are the true time lag values inferred from the AD model. The contour levels of the 2D joint probability densities are at the 1 σ and 2 σ regions.

baseline_v2.0_10yrs_5 days_r indicates that the metric is run on the observing strategy baseline, from the OpSim version 2.0, with a survey duration of 10 yr, and that the time lag to be probed by the metric is 5 days, in the LSST r band.

The v2.0 simulations were developed in response to the Survey Cadence Optimization Committee’s Phase 1 recommendations (Ivezić 2021). One of the most significant differences between previous survey simulations is that the baseline survey footprint has been slightly modified: the Wide Fast Deep area (WFD), which typically obtains on the order of 825 visits per pointing split across six filters, now explicitly includes a low-dust-extinction area as well as a Galactic plane extension.⁴³

First, we provide the overall analysis in Section 5.1, which makes use of our metric `AGN_TimeLagMetric` implemented in MAF. The DDFs (Brandt et al. 2018; Scolnic et al. 2018) are the most prominent locations for LSST RM, according to our initial analysis (Kovačević et al. 2021a). The existing baseline survey strategy contains five DDFs (Jones et al. 2020). Four of the DDF sites had been established for some time; the fifth field position is at present anticipated to overlap with the Euclid Deep Field South, which needs two LSST pointings to be covered entirely. The cadence of visits, as well as coadded depths of these DDFs, still needs to be finalized (Jones et al. 2020). The identifiers and equatorial coordinates of the DDFs are (see Jones et al. 2020): ELAISS1 (9°45′, −44°0′), XMM_LSS (35°71′, −4°75′), ECDFS (53°13′, −28°1′), COSMOS (150°1′, 2°18′), EDFS_a (58°9′, −49°32′), and EDFS_b (63°6′, −47°6′). Note that the Euclid Deep Field South (EDFS) is divided into two sections (see details in Capak et al. 2019; Cuillandre et al. 2021); but for the sake of brevity, we only refer to the five unrelated DDFs when a broad discussion is required. Then, armed with the best strategies, we aim to simulate photometric time lag recovery

as precisely as possible in Section 5.2. In our simulation, we chose a quasar redshift of $z=0.5$ as for higher redshifts a careful choice of bands covering the continuum is needed (see details in Jankov et al. 2022).

5.1. Assessment of Cadence Strategies Based on MAF Simulations

Here, we use our metric to investigate the impact of different cadence strategies on the study of AD time lag measurement. We performed a simulation using the `AGN_TimeLagMetric` in MAF as described in Section 4.1. We probed fiducial time lags of 1, 2, 3, and 5 days because they are close to the expected mean time delay for our transfer function model. Aitoff projection of our metric realization in MAF simulation for LSST cadences is shown in the Appendix (see Figures A1–A9).

In our analysis, we searched for the shortest possible time lag that could be measured reliably by RM in all bands. In this and the following subsections, we show that the best cadences for simultaneous⁴⁴ time lag measurements in the $ugriz$ bands are 5 day lags for the DDFs. Shorter time lags can be observed in the i and r filters in DDFs, as will be seen in zoomed-in plots of metric values later on in this section. This should not come as a surprise given that these bands may contain cadences that are somewhat more dense (Kovačević et al. 2021a). Longer time lags, $\gtrsim 7$ days, are detectable in each of the filters, as we shall show in the following that mean cadence samplings are favorable across bands. As it could be an issue that the optimal solution matches the upper limit of the probed time lags, we also tested these cadences by simulating RM measurements with shorter time delays in all bands.

Table 1 outlines some of the most important aspects of the LSST observing strategies used in this work. The baseline

⁴³ https://github.com/lst-pst/survey_strategy/blob/main/fbs_2.0/SummaryInfo_v2.0.ipynb

⁴⁴ The term simultaneity refers to the fact that our method determines all delays for the light curves quintet at the same time.

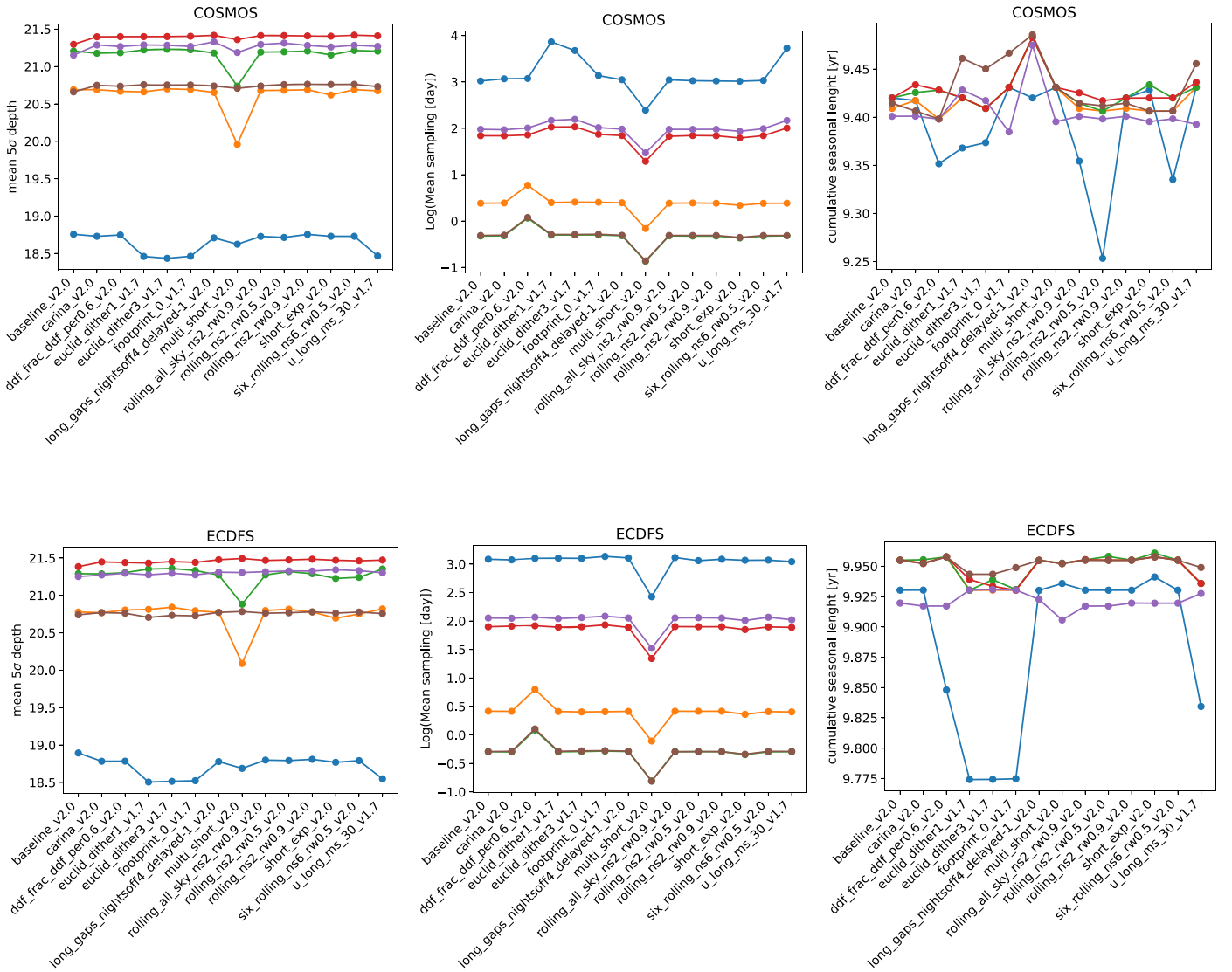


Figure 11. Comparison of mean 5σ depth (left column), mean sampling (middle column), and mean cumulative season length (right column) for different observing strategies (x -axis) in DDFs and $ugrizy$ filters. The solid lines guide the eye. The mean 5σ depths of the non- r and r bands are close. This means that objects as bright as 21 will still be seen in those bands for these overlapping cadences in DDF. Also, fainter objects in the non- r band will be observable in the r band. The passbands u , g , r , i , z , y are denoted with blue, orange, green, red, violet, and brown, respectively.

strategy (baseline_v2.0) features a modified⁴⁵ survey footprint with an expanded dust-free area and WFD-level visits in the Galactic Bulge and Magellanic Clouds. Coverage of the Northern Ecliptic Spur, South Celestial Pole, and remainder of the Galactic Plane is maintained, at lower levels. The existing baseline used 2×15 s exposures per visit, and most visits were in the same filter (although this was not enforced; Jones et al. 2020)⁴⁶. There are specific programs that, if given specialized observing time via “microsurveys,” can produce additional science outside or in support of the basic Rubin LSST science drivers. One such program is that included in the strategy carina_2.0 and is intended to observe the Carina nebula.⁴⁷ Both strategies show three prominent DDF fields-XMM_LIS close to equator, ECDFS below previous and

ELAISS1 close to polar axis (see Figure A1). For measuring time lags smaller than 5 days, carina cadences in the r and z bands show a very small area with Nyquist sampling or better at the sky location $\delta = 30^\circ$, $\alpha = 18$ –20 h of the LSST equatorial sky plane.

OpSims are using a custom dither pattern for the Euclid DDF to better match the Euclid field of view (EDFS_a, EDFS_b). Also, euclid_dither1 and euclid_dither3 exhibit three notable DDFs with moderate metric value in a tiny field at the position $\delta = 0^\circ$, $\alpha = 22$ hr (Figure A2). Figure A2(d) has an additional field of moderate metric value on the right side of the main vertical axis of sky symmetry at the position $\delta > 0^\circ$, $\alpha = 8$ hr. The footprint cadence strategy allows for various survey footprints based on increasing the low-extinction area of the WFD footprint. In all filters except the u -band filter, the cadence in the footprint strategy exhibits a limited region, which is shifting the location for time lags between 1 and 3 days (Figure A3). However, for the measurement of 5 day time lags in the i and r bands, the three DDFs (as in prior cadences) occur in of Figures A4(e) and (f).

⁴⁵ Filter balance is modified in different areas of the sky.

⁴⁶ As clarified by Jones et al. (2020): “A ‘visit’ here is an LSST default visit, which consists of two back-to-back 15 s exposures, for a total of 30 s of on-sky exposure time. These back-to-back exposures are always in the same filter, separated only by the 2 s readout time.”

⁴⁷ https://github.com/lst-pst/survey_strategy/blob/main/fbs_2.0/SummaryInfo_v2.0.ipynb

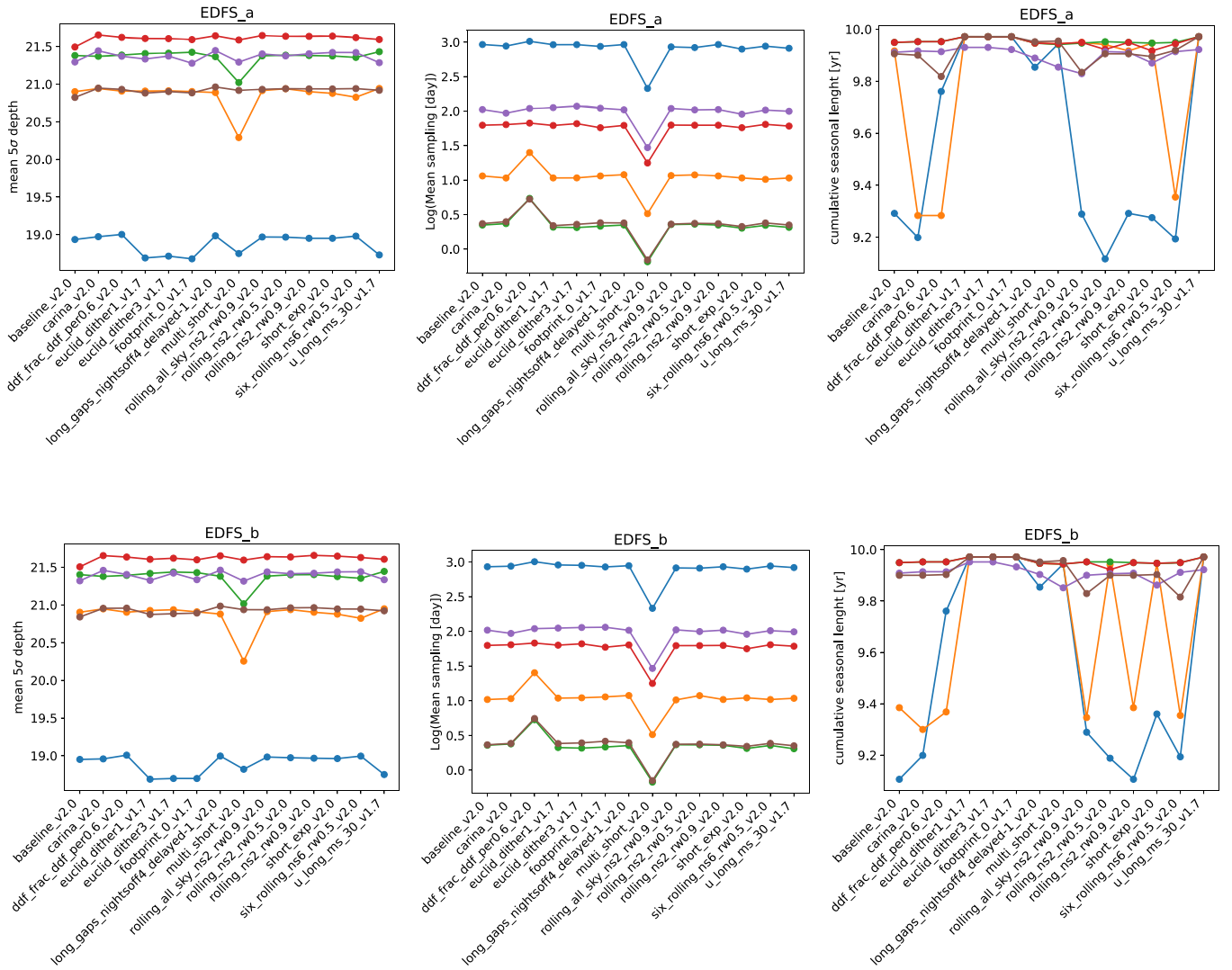


Figure 12. The same as Figure 11 but for different DDFs.

As the baseline survey strategies involve pairs of visits every few evenings, separated by around 33 minutes, `long_gaps` simulations include a third visit after a time interval of 2–7 hr. In the case of `long_gaps_nightsoff`, long gaps appear every seven nights starting after year five. DDFs are dominant in both the i and r bands for a measurement of 5 day time lags, which is comparable to prior occurrences in other metric realizations (see Figure A5).

Microsurveys `multi_short_v2.0` cadences emphasize multiple (four), short (5 s) exposures in each filter. For them, metric simulations show a distinct topology so that suitable fields are clustered in a wavy band that is almost parallel to the sky equator but with varying densities (Figures A6–A7). Among the metric realizations, the u band has the highest density of sky locations appropriate for RM; see Figure A6(d) and Figure A6(i), Figure A7(b) and Figure A7(g). The same three DDFs that were appearing in the prior cases are depicted in Figure A6(i) and Figure A7(h). Notably, four DDFs are found in Figure A7(e) and Figure A7(f).

The `rolling_all_sky_ns2` are two-band rolling all sky cadences with weights 0.5 and 0.9, where the metric realization is comparable to `long_gaps_nightsoff`, `footprint`, `carina` (see Figure A8) and `euclid_dither` (see Figure A9).

The microsurveys strategy `short_exp` takes up to three short (5 s) visits in year one. As illustrated in Figures A10–A11, the topology of the metric realization is comparable to that of the metric realization on `rolling_all_sky_ns2`, with the exception that the u band is more dominant.

As the updated baseline contains a two-band rolling cadence with strength $\sim 90\%$ in the dust-free WFD, `six_rolling_ns6_rw0.5` simulations modify this rolling cadence in the dust-free WFD to use six regions instead of two, with variable weight (“strength”) to the level of rolling. The `u_long_ms_30` cadences take u -band observations as single snaps, and test increased u -band exposure times, in this case 30 sections. Interestingly, metric realizations on `six_rolling_ns6_rw0.5` and `u_long_ms_30_v1.7` cadences (Figure A12) are as prevalent in DDFs as they are in the case of metric realizations on `euclid_dither` cadences.

The LSST Science Advisory Council report raised a series of questions and identified suggested simulation experiments to run. Among them are also listed Experiments with DDFs cadences (Jones et al. 2020). The observational cadence, which is currently being debated for the LSST DDFs (Jones et al. 2020), is indicated as one of the most critical elements that determines disk size measurements. The detailed investigation

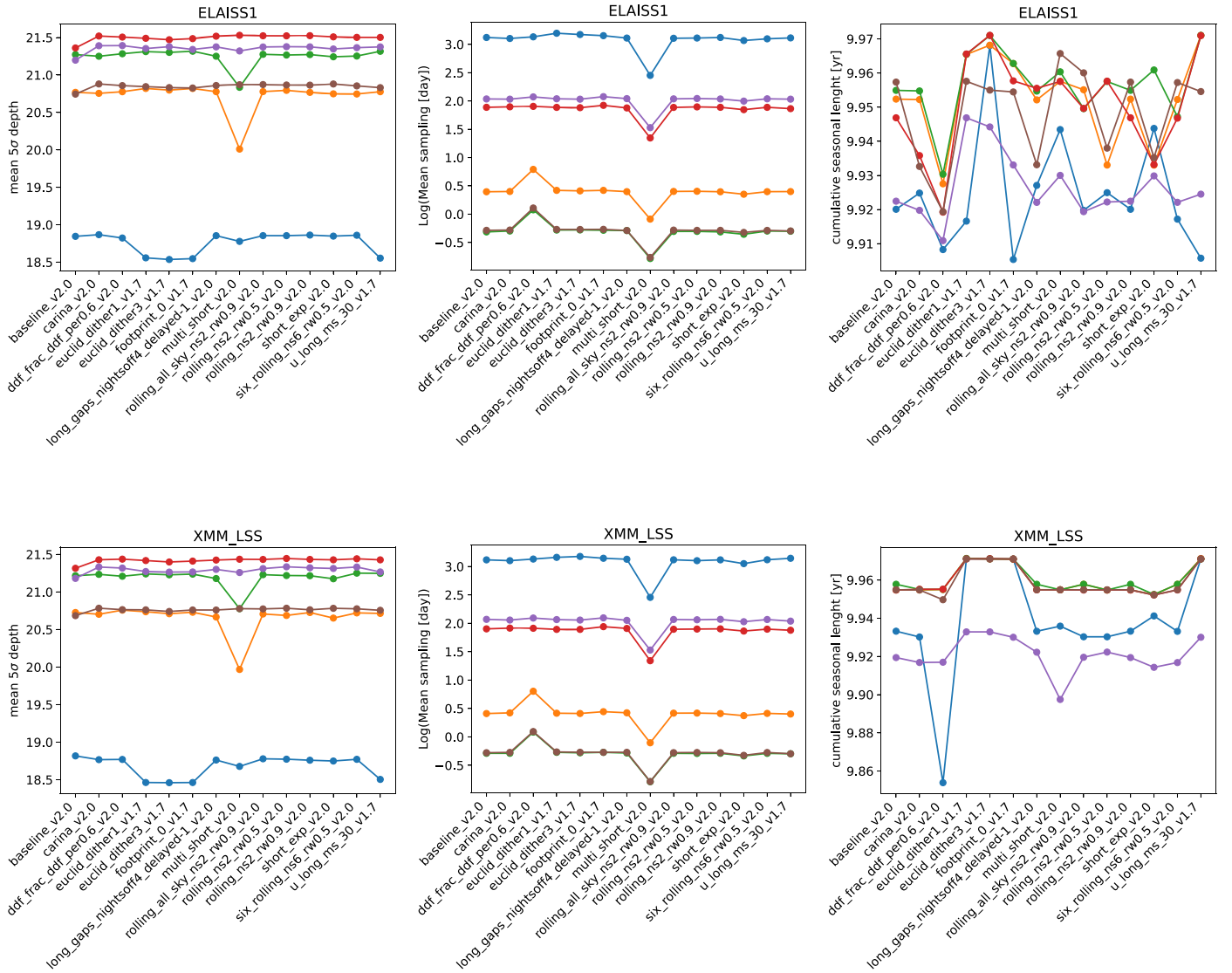


Figure 13. The same as Figure 11 but for different DDFs.

of the distribution of metric realizations (values above Nyquist criterion) on DDFs is shown in Figure 6. The highest-quality time lag measurement is predicted to be obtained using data from the COSMOS, XMM_LSS and ECDFS while the lowest-quality time lag measurement is expected to be obtained using data from the EDFs_a and EDFs_b fields. Notably, the metric value for the multi_short cadence in the u band is 20%–30% lower than the threshold. As we will see in the following sections on examples of multi_short cadence, cadences with metric values nearing the threshold could be adequate to calculate time delays. The coadded depth varies across different filters and observing strategies in each DDF as illustrated in Figures A13–A14. Currently, the deepest fields are ECDFS, XMM_LSS, and ELAISS1. Interestingly, the multishort strategy consistently produces the highest-quality time delays, and it also has the largest depth for all DDFs.

To demonstrate in greater detail the comparison shown in Figure 6, we perform MAF simulation in DDFs with significantly higher resolution (see Figures 7 and 8) than the original images in the Appendix. The HEALpygnomview is used to create the high-resolution plots. The center of each plot

comprises the point on the DDF itself (as mentioned above) plus a radius of 5° (this defines the slice utilized to run the metric). The image itself displays the resolution per pixel. The x -axis represents R.A., and the y -axis represents decl. The metric realizations are given in two 3×3 grids of panels. The metric outperforms in all DDFs with the exception of EDFs_a and EDFs_b.

Based on the similarity of the metric value distributions, there are three types of DDFs: homogeneous DDFs with the highest metric values (first panel in the top row and middle panel in the middle row in Figure 7), inhomogeneous DDFs with dispersed high metric values (second panel in the top row in Figure 7; second and third panels in the top and middle rows in Figure 8), and elliptically distributed DDFs (the last panel in the middle row in Figure 7; bottom rows in Figures 7 and 8). This example, on the other hand, clearly indicates that observations in elliptical regions can be coupled with equivalent partitions in homogeneous DDFs in a straightforward manner.

In summary, we found that when the overall cumulative observational season length is long (~ 9 yr), the lag measurement

Table 1
Overview of the LSST Cadence Strategies

(1)	OpSim (2)	Area with >825 Visits (deg ²) (3)	Area with Low Extinction (deg ²) (4)	N_{visit} Total (5)	Median N_{visit} (6)	Median N_{visit}	
						u Band (7)	g Band (8)
baseline	2.0	12,434.14	16,842.94	2,081,749.0	838.0	54.0	68.0
carina	2.0	12,519.74	16,385.53	2,087,222.0	838.0	54.0	70.0
multi_short	2.0	151.07	16,639.0	3,584,186.0	696.0	100.0	125.0
rolling_all_sky_ns2_rw0.9	2.0	12,900.78	16,599.55	2,088,105.0	839.0	54.0	69.0
short_exp	2.0	10,664.07	16,581.09	2,180,235.0	831.0	56.0	72.0
six_rolling_ns6_rw0.5	2.0	12,342.65	16,665.01	2,084,148.0	837.0	54.0	70.0
long_gaps_nightsof_delayed-1	2.0	10,288.90	15,954.13	2,067,452.0	830.0	50.0	70.0
euclid_dither1	1.7	17,982.71	15,174.43	2,045,493.0	888.0	55.0	79.0
euclid_dither3	1.7	17,967.60	15,161.84	2,045,144.0	888.0	55.0	78.0
footprint	1.7	15,390.97	16,492.96	2,046,219.0	853.0	52.0	72.0
u_long_ms_30	1.7	18,091.81	15,186.18	2,080,376.0	904.0	58.0	80.0

Note. A visit is currently defined to consist of two back-to-back 15 s exposures, for a total of 30 s of on-sky exposure time. These back-to-back exposures are always in the same filter, separated only by the 2 s readout time (Jones et al. 2020). From first to last column: observing strategy, OpSim version, the amount of area of WFD that receives at least 825 visits per pointing, the amount of area of WFD with low extinction, total number of visits per point on the sky, the median number of visits that the most frequently visited 18,000 square degrees receives, and the median visits distributed per the u and g band. More details are given in a collection of information relevant for survey strategy https://github.com/lsst-pst/survey_strategy. The cadence of visits, as well as coadded depths of DDFs, still needs to be finalized.

likelihood increases because the multiband continuum light curves can track more light-curve features. However, survey cadence strategy is also necessary for lag recovery because sampling the accretion disk light curves at the Nyquist frequency is required to resolve the lag accurately. As a result, objects having an estimated FWHM of the AD transfer function less than the minimum sampling are less likely to have a meaningful lag estimate. Larger gaps can be tolerated as long as the cadence is small and a long period can be covered, as proven by time lag measurements utilizing the COSMOS and ECDFS field cadence strategies indicated by our metric.

5.2. Effective Time Lag Measurement

Here, we further quantify the potential of measuring time lags using simulated LSST light curves for a subset of the best observational cadences as suggested by our metric realizations: the two DDFs (COSMOS and ECDFS) observed in `multi_short_v2.0_10yrs` cadence in the $ugrizy$ bands.

We use typical parameters for quasars having median characteristics (SMBH mass $M = 2 \cdot 10^8 M_{\odot}$, $L/L_{\text{Edd}} \sim 0.1$, $\eta = 0.1$, disk inclination of 45° , azimuth angle of 0°), characteristic DRW timescale $\tau_{\text{DRW}} \sim 200$ days and a structure function at infinity $\sigma_{\text{DRW}} = 2.5$, because we are interested in quantifying the performance of time lag measurement on a `multishort` cadence (having multiple (four) short (5 s) exposures in each filter).

To create simulated light curves, we first produce the observation schedule and depth of each epoch using the LSST OpSim (Delgado & Reuter 2016). In each DDF, we created a suite of quintets of multiband light curves by a convolution of the AD transfer function with the DRW driving light curve (see Section 3.2).

Examples of quintets for each DDF are given in Figure 9. The warping of light curves in different bands, due to transfer function skewness, is evident. For example, warping can be seen in ELAISS1 DDF around MJD 61000 during one observational season. The photometric noise in all light curves is set to 0.005 mag (i.e., at the level of 0.02% as the best

scenario found in our white paper⁴⁸ thorough simulations; Kovačević et al. 2021b). The first row in Table 2 lists the true values of AD time lags $\tau_{ij} = \langle \tau \rangle_j - \langle \tau \rangle_i$, $j \in (g, r, i, z)$ as calculated from Equation (5). The remainder shows estimates using our procedure to determine time lags of the light-curve quintets (see Section 4.2 for details).

The estimated 1D probability distribution for each time lag and the joint probability distribution for each pair of time lags are shown in Figure 10. We see that the inferred values of the time lags are both accurate (close to true values) and precise (narrow posterior distribution) for ECDFS light curves in the g , r , and i bands. However, the PDF of τ_{ug} is deformed for COSMOS. In general, we see from the 1D histogram of Figure 10 that PDF intervals are much narrower than the prior ranges (see Section 4.2). Table 2 lists the mean of the posterior and uncertainties corresponding to 16th and 84th quantile of the distribution of measured time lags. Because light-curve distortion can make detecting delays in individual segments of light curves difficult, the AD time lag measurement is demonstrated on a decadal observational time baseline (see, e.g., Chan et al. 2020).

The light curves in the OpSim observation schedules have breaks between a series of continuous observations, with the gaps ranging from several days to ≥ 80 days. To see how these gaps affect lag measurements, we created additional ideally sampled simulated light curves with homogeneous sampling of 1 and 5 days.

By examining the corner plot for recovered time lags of 1 and 5 day homogeneous light curves (right panel in Figure 10), we conclude that the lag distributions are affected by homogeneous sampling. For the 1 day sampling, the PDFs are narrower and more symmetric with respect to true values. Table 2 presents summary statistics of distribution of time lag measurement on these ideally sampled quintets of light curves.

⁴⁸ https://github.com/LSST-sersag/white_paper/blob/main/data/table_1.pdf

Table 2

Summary Statistics of Recovered Time Lags from the Distributions for COSMOS, ECDFS, and Homogeneously Sampled Light Curves Given in Figure 10

Status (1)	LC Sampling (2)	τ_{ug} (3)	τ_{ur} (4)	τ_{ui} (5)	τ_{uz} (6)
True	...	0.653	1.514	2.388	3.177
Inferred	COSMOS	$0.643^{+0.06}_{-0.04}$	$1.507^{+0.027}_{-0.02}$	$2.388^{+0.029}_{-0.033}$	$3.166^{+0.017}_{-0.012}$
Inferred	ECDFS	$0.650^{+0.008}_{-0.008}$	$1.540^{+0.012}_{-0.08}$	$2.377^{+0.017}_{-0.022}$	$3.168^{+0.012}_{-0.009}$
Inferred	1-day	$0.649^{+0.01}_{-0.01}$	$1.508^{+0.01}_{-0.01}$	$2.388^{+0.04}_{-0.04}$	$3.168^{+0.01}_{-0.01}$
Inferred	5-day	$0.649^{+0.01}_{-0.01}$	$1.516^{+0.03}_{-0.04}$	$2.369^{+0.02}_{-0.03}$	$3.167^{+0.01}_{-0.01}$

Note. The columns are: status of time lags, light-curve sampling, the time lags of g -band versus reference u -band light curves; r -band vs. u -band light curves; i -band versus u -band light curves; and z -band vs. u -band light curves. True values of mean relative time delays $\langle \tau \rangle_{uj}$, $j \in (g, r, i, z)$ calculated from AD model (see Equation (5)). The inferred values represent the 50th quantile with errors corresponding to 16th and 84th quantiles of the respective probability distributions of calculated time lags.

Barth et al. (2011) have shown that for interpolation and cross-correlation methods applied to real data, as long as the driving light curve is well sampled (in their case, almost nightly over the course of 200 days), poorer sampling of the output light curves can be tolerated. We recall that, to first order, the centroid of the transfer function is simply proportional to the luminosity-weighted radius (Koratkar & Gaskell 1991). However, in the case of LSST multiband continuum transfer functions, their centroids are shifted closer to their FWHM (see Figure 3). Also, we see that interband continuum delays that are driven by DRW have values below or close to transfer function centroids (e.g., Figure 10). So, it is important to have a sampling that is of the order of the FWHM of the AD transfer function. This condition is most relevant for measuring the time lag between u -band and g -band light curves, as their interband time delay is the smallest.

6. Discussion

Our MAF metric (AGN_TimeLagMetric) indicates that the best cadences (i.e., those with the largest values above the Nyquist threshold) in the DDFs are those in the `multi_short` family, taking into account fiducial time lags of 5 days in all LSST filters. This family of strategies belongs to the microsurveys. Microsurveys aim to support and extend the LSST’s primary science drivers, and they were submitted in response to the 2018 Call for White Papers (see Bianco et al. 2022). Many of the microsurveys requiring between 0.3% and 3% of the overall survey time were simulated as part of `OpSim v2.0` simulations. The `multi_short` takes four short (5 s) exposures in each filter, which is about 20 s in total per filter. Despite the short exposure time, the high observational cadence allows for photometric RM analysis as indicated by our simulations as well as other studies (see Yu et al. 2020). However, when considering microsurveys, it is worthwhile to note that sometimes visits can be extremely short, which can affect RM observables. The DDFs currently receive about 1% of the total survey time per DDF location. There are five DDFs, so this accounts for 5% of the total survey time. Each DDF is a single pointing, with the exception of the Euclid South DDF, which consists of two shallower pointings.

However, there are simulations where the amount of time allocated for DDFs is varied from 3% (`ddf_fract_ddf_per0.6_v2.0_10yrs`) to 8% (`ddf_fract_ddf_per1.6_v2.0_10yrs`). Our MAF simulations show that there is no significant difference between these two variants of DDFs when it comes to time lag measurements.

From our simulations (see also Kovačević et al. 2021b), we find that the most important parameters that affect the quality of time delay measurements in AGN ADs are the cumulative season length and the mean sampling (also referred to as the sampling frequency). A categorization of 14 observing strategies in all DDFs and LSST filters, based on mean 5σ depth, mean sampling, and mean cumulative season length, is shown in Figures 11–13.

The mean cumulative season length, mean sampling, and mean 5σ depth from a simulation of a given observing strategy are calculated by taking the mean of these parameters for the DDF under consideration (Figures 11–13). The cumulative season length is the sum of the duration of all observing seasons. A season gap for an LSST field is defined as no observations in any filter taking place for 85 days (Huber et al. 2019). Across all DDFs, the cumulative season length for the majority of strategies is ≥ 9.5 yr. We note that `multi_short` strategy has the fastest (smallest) sampling but the mean 5σ depth is shallower. The mean sampling exhibits a similar pattern of behavior per filter throughout all DDF fields, with subtle variations. Figure 11 shows the COSMOS field as an example. The mean sampling for some of the observing strategies in the u band in the COSMOS differs from other fields (e.g., compare mean sampling for families between `carina` and `footprint` in COSMOS and ECDFS; see Figure 11), which is related to time spent on other surveys such as the northern hemisphere, the southern Celestial Pole, and the Galactic Center. As seen in Figures 11–13, the y band has the best mean sampling; yet, y -band light-curve distortion is the greatest due to AD transfer function asymmetry, making determining the time lag problematic (not impossible, but with the largest error). Thus, for simplicity, we do not consider the y -band lags.

We underline that our metric pointed to those strategies that would be appropriate for AD time lag measurements of the order of 5 lt-days, which is a severe limitation. We investigated alternative cuts for 5σ magnitude depth for brighter ($r < 21$, $g < 22$) and fainter ($r > 21$, $g > 22$) sources. Adding a cut for 5σ depth in the r band < 21.0 implies that the (vast majority) of visits with $r > 21.0$ will not be counted, but objects as bright as 21 in the r band will still be detectable; on the other hand, using a cut of $r < 21$ implies that only visits with a very limited depth will be available (Jones, private communication). However, no significant adjustments have been made in the overall analysis, as strategies with mean 5σ depth $r \sim 20$ –21, $g \sim 20$ –21 have been chosen.

Next, we obtain the differential number distribution of quasars with possible time lag measurements with respect to the u band by integrating the time lag measurement distribution over the source population:

$$\frac{dN}{dz} = \int_L^\infty dL \frac{d^2N}{dLdV} \Omega \frac{dV}{dz} p_\tau$$

where $\frac{d^2N}{dLdV}$ is a QLF, Ω is the fiducial survey area, and p_τ is the probability of a time lag measurement as defined in Section 2. We generated time lags using our AD model for 200 uniformly distributed SMBH masses ($10^6, 10^{10}M_\odot$) over 200 equal bins ($dz \sim 0.035$) of redshifts ($z \sim 0-7$). The total number of quasars for which time lags could be measured is

$$N = \int \frac{dN}{dz} dz.$$

In Figure 14, we plot the expected number of quasars (in 10 deg^2 survey area) for which it will be possible to measure time lags in the main LSST bands simultaneously assuming a fiducial cadence ~ 1 day as a function of redshift. The steepness of these number counts is shallower for the u band than for other bands, implying that for time lag measurements using the u band, the survey area is far more relevant than the redshift. Total counts will decrease in the same proportion as cadence increases. As a result, the estimated number of quasars for a 5 day cadence will be five times lower than for a 1 day cadence. We emphasize that this is an upper-bound (i.e., optimistic) estimate of the expected number of quasars with possible time lag measurements.

Also, we approximate the total number of quasars whose time lag could be detected in a DDF (in any filter) at a confidence interval (CI) assuming an accuracy of the time lag estimate of at least $\Delta = 10\%$ for blind search (no data about mass and redshift) as:

$$N \sim CIN_{\text{rep}} \Delta \frac{\Omega_{\text{LSST}} t_{\text{LSST}}^{\text{cum}}}{\Omega_{\text{rep}} t_{\text{rep}}^{\text{cum}}},$$

where $N_{\text{rep}} \sim 344$ is the number of quasars in VST COSMOS estimated by De Cicco et al. (2021), $\Omega_{\text{LSST}} \sim 10 \text{ deg}^2$ is a fiducial element of LSST area, $\Omega_{\text{rep}} \sim 1 \text{ deg}^2$ is an area associated with N_{rep} , and $t_{\text{rep}}^{\text{cum}} \sim 3 \text{ yr}$ and $t_{\text{LSST}}^{\text{cum}} \sim 10 \text{ yr}$ are the mean cumulative season lengths for VST COSMOS and LSST, respectively. Then the number of quasars for which time lags will be determined at least at CI ~ 0.95 and with an accuracy rate $\Delta \sim 0.1$ is $N \sim 1089$ per 10 deg^2 in any filter.

Time lags measured with the actual DDF cadences are less accurate and precise than those estimated using homogeneously sampled light curves (see Figure 10). For instance, we see that the COSMOS and ECDFS PDFs are more skewed than for homogeneously sampled light curves. Furthermore, the PDF of measured time lags can be bimodal, as found for r -band light curves in ECDFS. This is not surprising given that our metric shows that r -band sampling in ECDFS is of lower quality than in COSMOS, whereas it is the same for other bands (see Figure 6). While the secondary peak on the left is much closer to the true value, it is also much less probable. We showed that using a shifting algorithm with a light-curve similarity measure based on area and arclength might yield temporal lag uncertainties in DDFs of the order of 10% or less (see Table 2). RM measurement errors are anticipated to be more

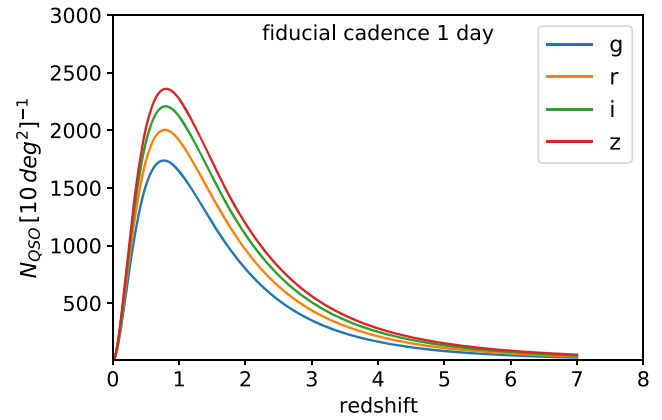


Figure 14. The expected number of quasars for which time lag could be measured with respect to the u band, in the main LSST filters as a function of the redshift, for fiducial 10 deg^2 survey area and fiducial cadence of 1 day.

tolerable in the DDFs, where sampling is expected to be an order of magnitude denser than in the main survey. By modeling many different observation tactics for the LSST DDFs, Yu et al. (2020) discovered that changing the cadence from 3 days to 1–2 days should greatly improve the yield of accretion disk size measurements. This is in accordance with other studies on RM. For example, typical time lag errors of $\sim 30\%$ are typically reported by spectroscopic reverberation experiments (Haas et al. 2011; Pozo Nuñez et al. 2015). Note as well that estimated uncertainties of 30% for undersampled data may be optimistic (Haas et al. 2011). Enhanced sampling for a spectroscopic reverberation campaign on NGC 4051 revealed that its BLR size is actually a factor of three lower than previously assumed from undersampled data (Denney et al. 2009). Thus, with well-sampled LSST reverberation data, the time lag estimations can be improved, and tensions with theoretical estimates may be resolved.

It has been reported that curve-shifting algorithms sensitive to sharp features and operating on the same timescales as the transfer function underestimate multiband time delays by up to 20% (Chan et al. 2020). However, using machine-learning methods for a similarity measure of light curves that do not require the same length and number of points, such as PCM, could be advantageous for LSST RM. Our preliminary tests show that using curve similarity measures has the potential to improve time lag determination so that typical errors might be within 1%–10% (see Table 2).

Because the disk variability for type I AGNs is almost unobscured, measuring intercontinuum delays for these objects will be easier than for type II (due to longer variability timescales and smaller variability amplitudes).⁴⁹ The LSST will also increase the number of type I AGNs, and low-luminosity AGNs with smaller black hole masses, so that shorter continuum delays will become more common. As the magnitude of optical variability on the order of \sim days could be anticorrelated with SMBH mass and AGN luminosity (Kelly et al. 2013), perhaps AGNs with smaller black hole masses will be better candidates for lag measurements (see also Yu et al. 2020).

An alternative to intensive high-cadence monitoring of a small number of objects is to follow up a larger sample of

⁴⁹ If type I Seyferts are host dominated, this issue may be applied to them as well.

objects at a cost of a lower cadence. While individual objects are unlikely to provide high-fidelity lag-wavelength relationships, a large population of objects can be analyzed as a whole (see, e.g., Jiang et al. 2017; Mudd et al. 2018; Homayouni et al. 2019; Yu et al. 2020). Both Homayouni et al. (2019) and Yu et al. (2020) reported disk sizes that are consistent with the standard disk model, whereas Homayouni et al. (2019) demonstrated that if only the best lag measurements are used, disk sizes are skewed to be higher than when the entire sample is taken into account. However, the multiband AD light curves are warped due to transfer function skewness. We demonstrate that when light curves are denser, as in the case of DDF, where sampling approaches the width of their transfer functions, the results are better. The u -band light curve has the shortest wavelength and the smallest width of the transfer function, implying that its higher cadence is very desirable. However, in order to examine X-ray to UV delays, the sample density of light curves in all bands should be greater than the width of their transfer function (see Kammoun et al. 2021).

Accretion disk investigations have been challenged by the fact that observations of their sizes are consistently larger than expectations from the thin-disk model by factors ranging from two to three (Chan et al. 2020). For an accurate measurement of disk size, it is necessary to take into consideration the appropriate transfer functions (Starkey et al. 2016; Chan et al. 2020). DDFs (Brandt et al. 2018; Scolnic et al. 2018) where substantial multiwavelength observations have been collected from earlier surveys (De Cicco et al. 2021) will be of greatest interest for detecting time lags by using these previous data to constrain the transfer functions. There are ongoing efforts of creating a prime sample of quasars to further test the applicability of the DRW model and the stationarity of the stochastic variability process. Stone et al. (2022) investigated the optical continuum variability of 190 quasars within the SDSS Stripe 82 over 20 yr long baseline. This sample contains hundreds of epochs from SDSS, PanSTARRS-1, the Dark Energy Survey, and dedicated follow-up photometric monitoring with DECam on the CTIO-4 m Blanco telescope, making it one of the best-quality light-curve data sets for studying quasar variability. Monitoring of this sample is a continuous endeavor to photometrically monitor deep extragalactic fields and collect a large amount of multiwavelength and time-domain data (Stone et al. 2022). Extension of the baseline by another 5 yr will allow these light curves to be smoothly combined with LSST data, so that this quasar sample will be premier for studying optical continuum variability.

We also briefly discuss the relation of our analysis to an important methodological study by Hu & Tak (2020) on multiband GP, the motivation of which is consistent with this work. Assuming correlations of the characteristic timescale (τ) and an asymptotic rms variability on long timescales (SF_∞) among bands, they proposed a multivariate DRW model for modeling AGN light curves in five bands and with irregular cadences. Similar to our study, Hu & Tak (2020) first generated simulated light curves with measurement errors using the DRW model. Then Hu & Tak (2020) applied the univariate and multivariate DRW model on simulated light curves and an SDSS spectroscopically confirmed quasar, and found that the multivariate model can help reveal the possible correlations of true timescales across five bands and time delays between doubly lensed multiband light curves. Although our analysis does not include the more rigorous multiband GP time lag

method, the time lag method in our study is sufficient for demonstrating RM within various OpSim runs in terms of optimizing observing cadence and strategy.

7. Final Remarks

In this paper, we introduced a metric incorporated in MAF that quantifies the accuracy of LSST observational strategies for AGN continuum time lag measurements. Our metric relies on the Nyquist sampling criterion, which is advantageous when discerning information on small-scale structures via electromagnetic signals. This enables us to identify specific LSST sky regions (compiled in an atlas) where observing strategies of high quality (satisfying the Nyquist criterion) could be effective for probing continuum time lags on scales of the AD and the transfer function.

A prominent example that will necessitate such spatial scales and will be explored in the future is the possibility that most observed continuum lags are driven by variable diffuse BLR emission rather than the irradiation disk (see Netzer 2022). We anticipate that light curves obtained from fields indicated by our metric will be useful for resolving what happens on long timescales and how it diverges from the lamppost model (Neustadt & Kochanek 2022).

Unlike the spectroscopic approach, photometric RM does not typically allow the BLR emission line and continuum light curves to be separated. Under certain conditions, separation of these processes is possible so the lag can be measured (see details in Chelouche & Daniel 2012; Chelouche et al. 2012). LSST sky regions selected by our metric will be ideal for testing the photometric RM methodology on LSST data (Jankov et al. 2022).

It is also interesting to consider what deep-learning algorithms (see, e.g., Tachibana et al. 2020; Čvorović Hajdinjak et al. 2022) might reveal when trained on multicolor higher cadence data in optimal LSST sky regions (as defined by our metric). Another feature of our metric is that it can be simply converted to probability and hence combined with other metrics such as quasar counts (Assef et al. 2021a).

The following is a brief summary of our work:

1. We compiled a comprehensive atlas of estimates of the performance of continuum—continuum time lag measurements as a result of our metric simulation conducted on MAF. The metric points out as the best strategies those found in DDFs. The `multi_short` strategy has the best sampling ($\lesssim 5$ days), but the mean 5σ depth is shallower.
2. To illustrate our finding, we simulate light curves using an AGN model based on a combination of thin-disk, lamppost, and DRW for the driving function. We estimate the time lags using shifting method inspired by PyCS but with the PCM method to determine the similarity between curves and identify a time delay measurement through minimization of PCM. Even with inferior sampling quality, like in the r band of ECDFS, the time lags could be determined with an accuracy of $\sim 10\%$.
3. Using our metric together with the artificially generated sample of quasar masses and their QLF, we predicted an upper bound of total quasar counts within $0 < z < 7$ for which their time lags might be measured. We estimate that time lag measurements leading to AD size measurements for more than 1000 sources in each DDF per 10

deg^2 in any filter will be possible. We found that the `baseline` family is suboptimal in all DDFs, as our metric is below the threshold in the g and z bands. Similarly, the `rolling` family underperforms in the r and g bands. In contrast, the `good_seeing` family of cadences is mainly moderate for determining time lag in all DDFs.

4. Based on preliminary numerical results, we propose that, in addition to methods that take into account the transfer function form in detail, LSST continuum RM can apply deep-learning techniques of similarity measures to potentially improve the time lag measurement process.

We sincerely thank Rachel Street, Federica Bianco, Gordon T. Richards, and William N. Brandt for their essential efforts in coordinating work on cadence evaluation within the Rubin-LSST Science Collaborations. This work was conducted as joint action of the Rubin-LSST Active Galactic Nuclei (AGN) and Transients and Variable Stars (TVS) Science Collaborations. The authors express their gratitude to the Vera C. Rubin LSST AGN and TVS Science Collaborations for fostering cooperation and the interchange of ideas and knowledge during their numerous meetings. The authors would like to thank the Vera C. Rubin Observatory MAF team, specially Lynne Jones, for their significant support in designing and integrating our metric into MAF. The authors warmly acknowledge the LSST Corporation's efforts to train and educate metric teams through many cadence tuning workshops and hackathons. This work was supported by the Preparing for Astrophysics with LSST Program, funded by the Heising Simons Foundation through grant 2021-2975, and administered by Las Cumbres Observatory.

A.B.K., D.I., I.J., I.Č.-H., L.Č.P., and V.R. acknowledge funding provided by University of Belgrade-Faculty of Mathematics (the contract 451-03-68/2022-14/200104), through the grants by the Ministry of Education, Science, and Technological Development of the Republic of Serbia. A.B.K. and L.Č.P. thank the support by Chinese Academy of Sciences President's International Fellowship

Initiative (PIFI) for visiting scientist. B.C. and S.P. acknowledge the financial support from the Polish Funding Agency National Science Centre, project 2017/26/A/ST9/-00756 (MAESTRO 9) and MNiSW grant DIR/WK/2018/12. C.R. acknowledges support from the Fondecyt Iniciacion grant 11190831 and ANID BASAL project FB210003. D.I. acknowledges the support of the Alexander von Humboldt Foundation. H.L. acknowledges a Daphne Jackson Fellowship sponsored by the Science and Technology Facilities Council (STFC). U.K., J.K.D., L.Č.P., M.L., O.V., and S.M.M. acknowledge funding provided by Astronomical Observatory (the contract 451-03-68/2022-14/200002), through the grants by the Ministry of Education, Science, and Technological Development of the Republic of Serbia. R.J.A. was supported by FONDECYT grant No. 1191124 and by ANID BASAL project FB210003. P.S.S. acknowledges funds by ANID grant FONDECYT Postdoctorado No. 3200250. S.P. acknowledges financial support from the Conselho Nacional de Desenvolvimento Científico e Tecnológico (CNPq) Fellowship (164753/2020-6). S.S. acknowledges funding provided by the University of Kragujevac—Faculty of Sciences (the contract 451-03-68/2022-14/200122) through the grants by the Ministry of Education, Science, and Technological Development of the Republic of Serbia. Y.R.L. acknowledges financial support from the National Science Foundation of China through grant No. 11922304 and from the Youth Innovation Promotion Association CAS.

Appendix

Atlas of Metric AGN_TimeLagMetric Simulation

Figures A1–A12 show the metric yield for different cadences on LSST observable sky. Figures A13 and A14 show the summary of coadded depths in DDFs for different observing strategies in the u , g , r , i , and z , y filters, respectively.

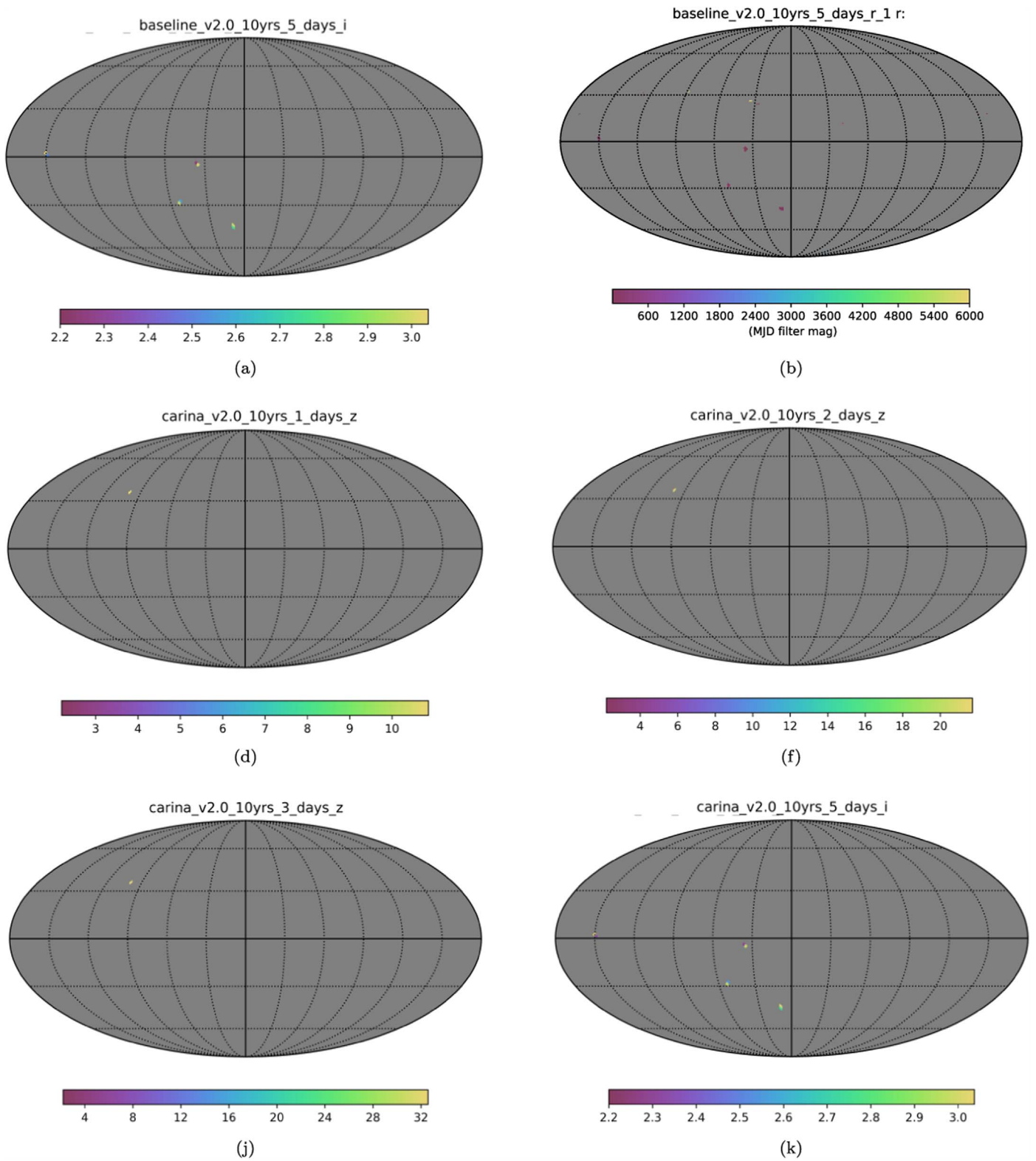


Figure A1. Metric realization for cadences from *baseline* and *carina* observing strategies for observed time lags of 1, 2, 3, and 5 days. The color bar displays metric values above the Nyquist threshold, which have been scaled for improved visual presentation in the Aitoff projection of celestial coordinates.

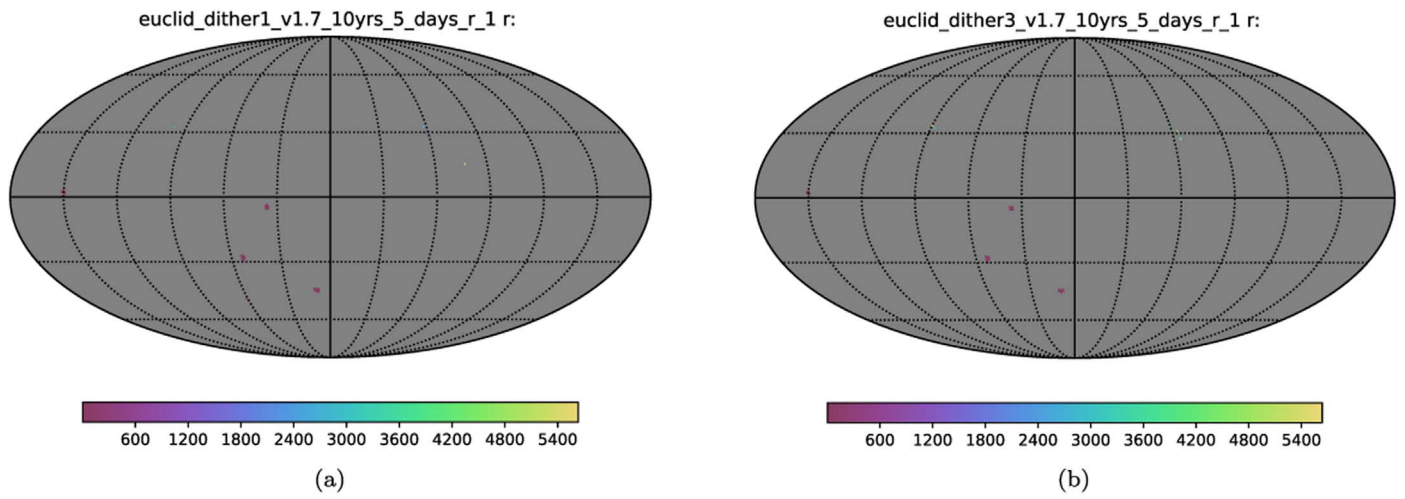


Figure A2. The same as Figure A1 but for `euclid_dither1` and `euclid_dither3` observing strategies. In all metric simulations, three DDFs stand out. For better color visibility in the right column, the metric threshold is multiplied by XXX.

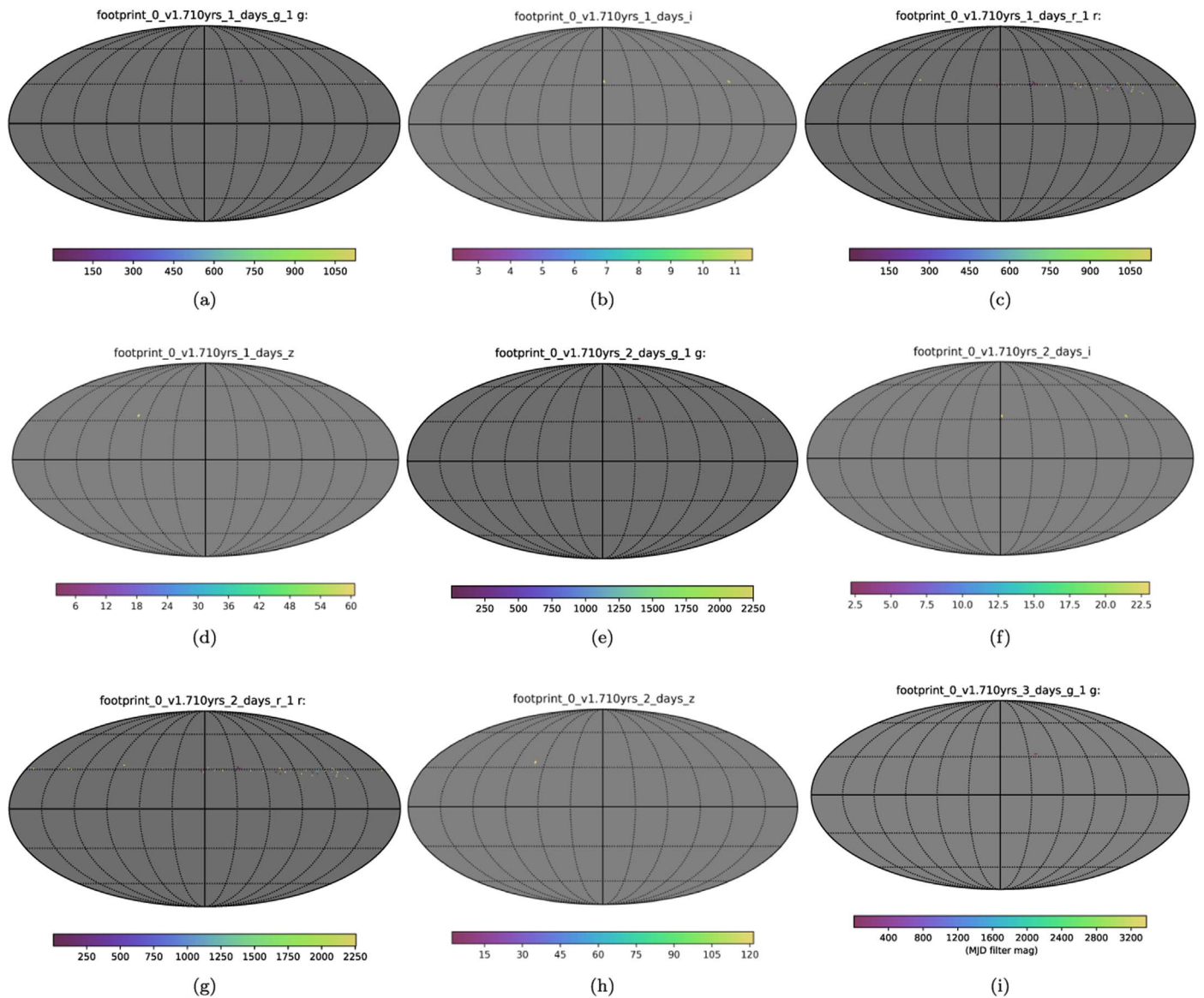


Figure A3. Metric realization from `footprint` observing strategies. There is only one prominent field in each panel (except panel (g)) slightly varying in position on the sky.

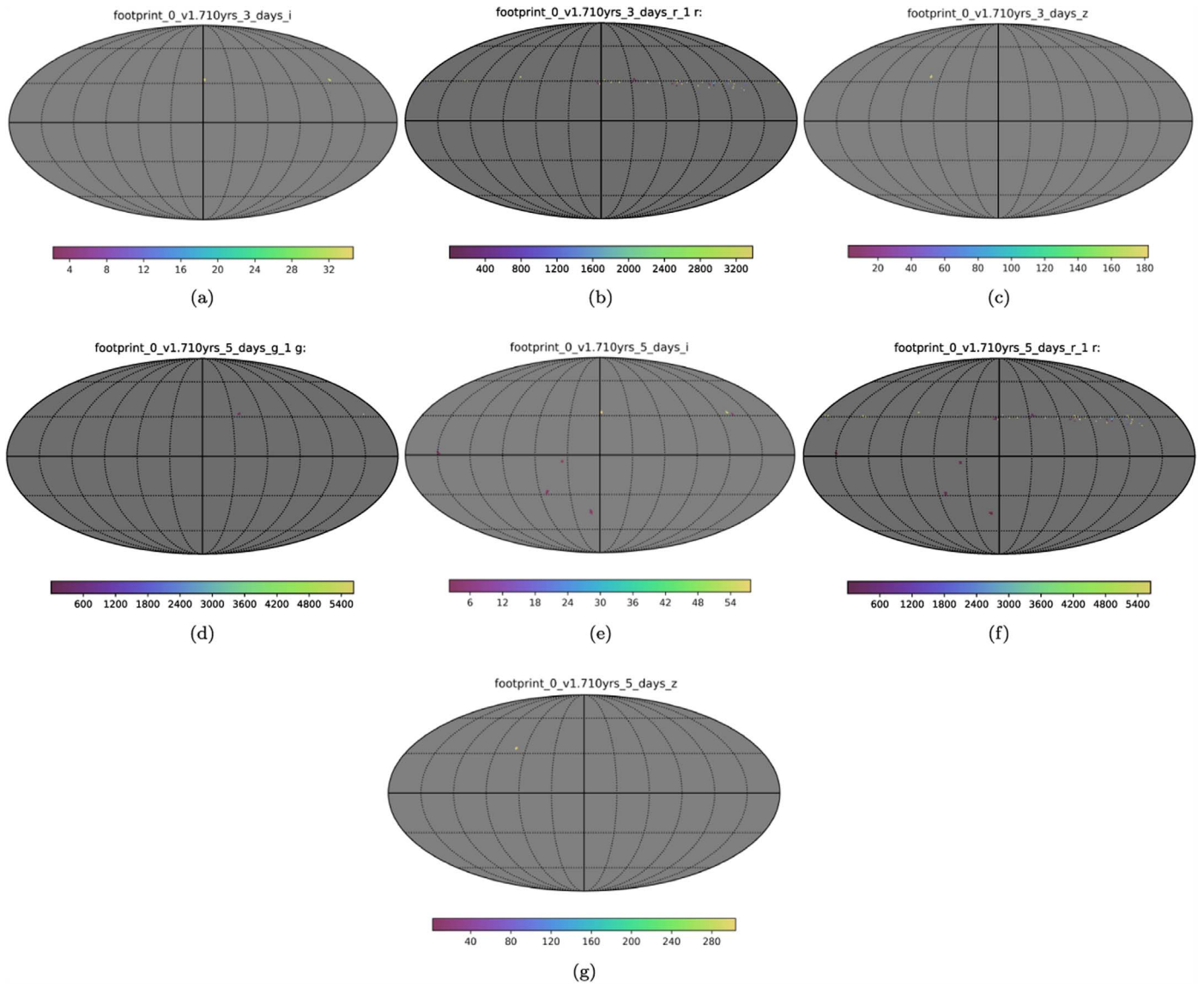


Figure A4. Metric realization for cadences from footprint observing strategies, continued. In contrast to Figure A3, DDFs appear in panels (e) and (f).

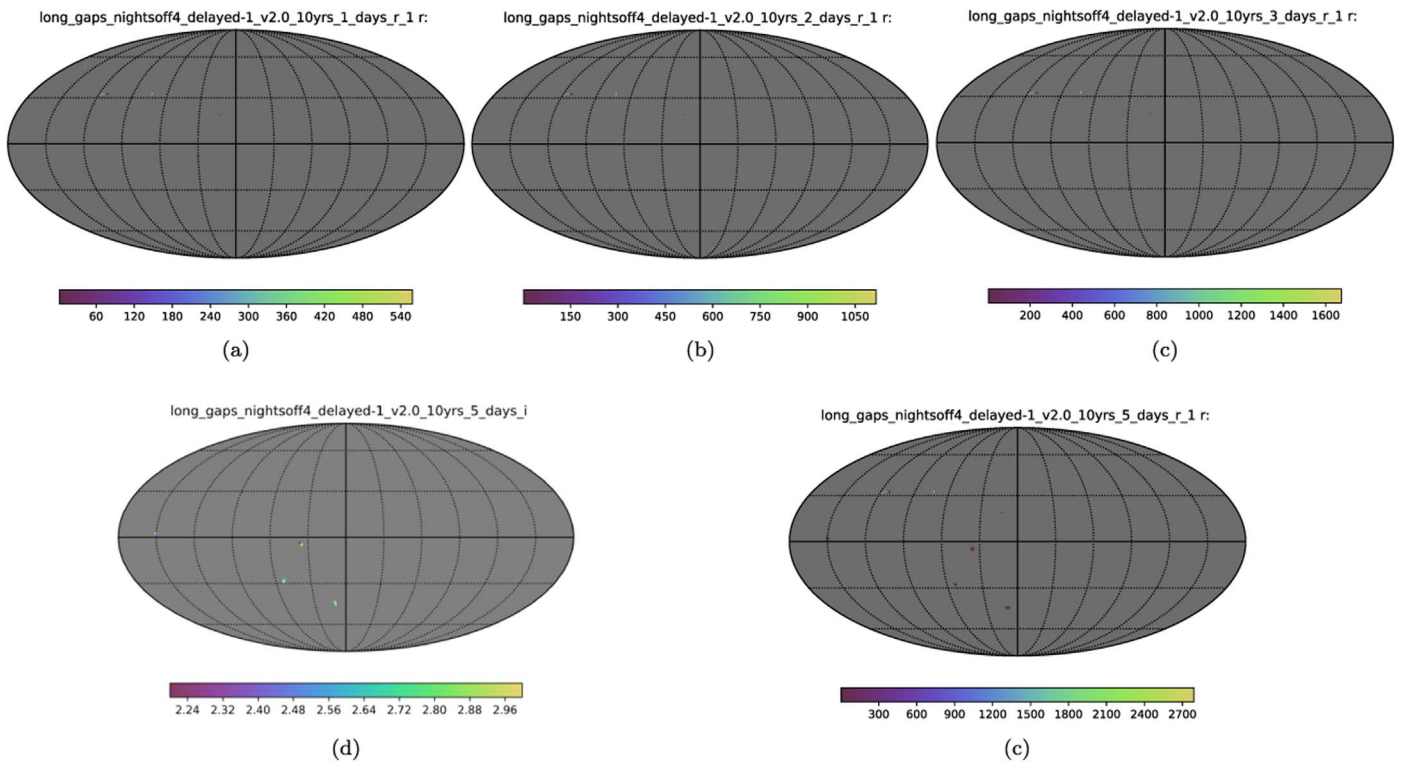


Figure A5. Metric realizations on cadences from `long_gaps_nightsoff` observing strategy. The first row of panels shows the fields (in the third and fourth area from the left of the main meridian) suitable for calculating 1–3 day delays. DDFs appear in the bottom row with better metric realization in the *i* band than in the *r* band.

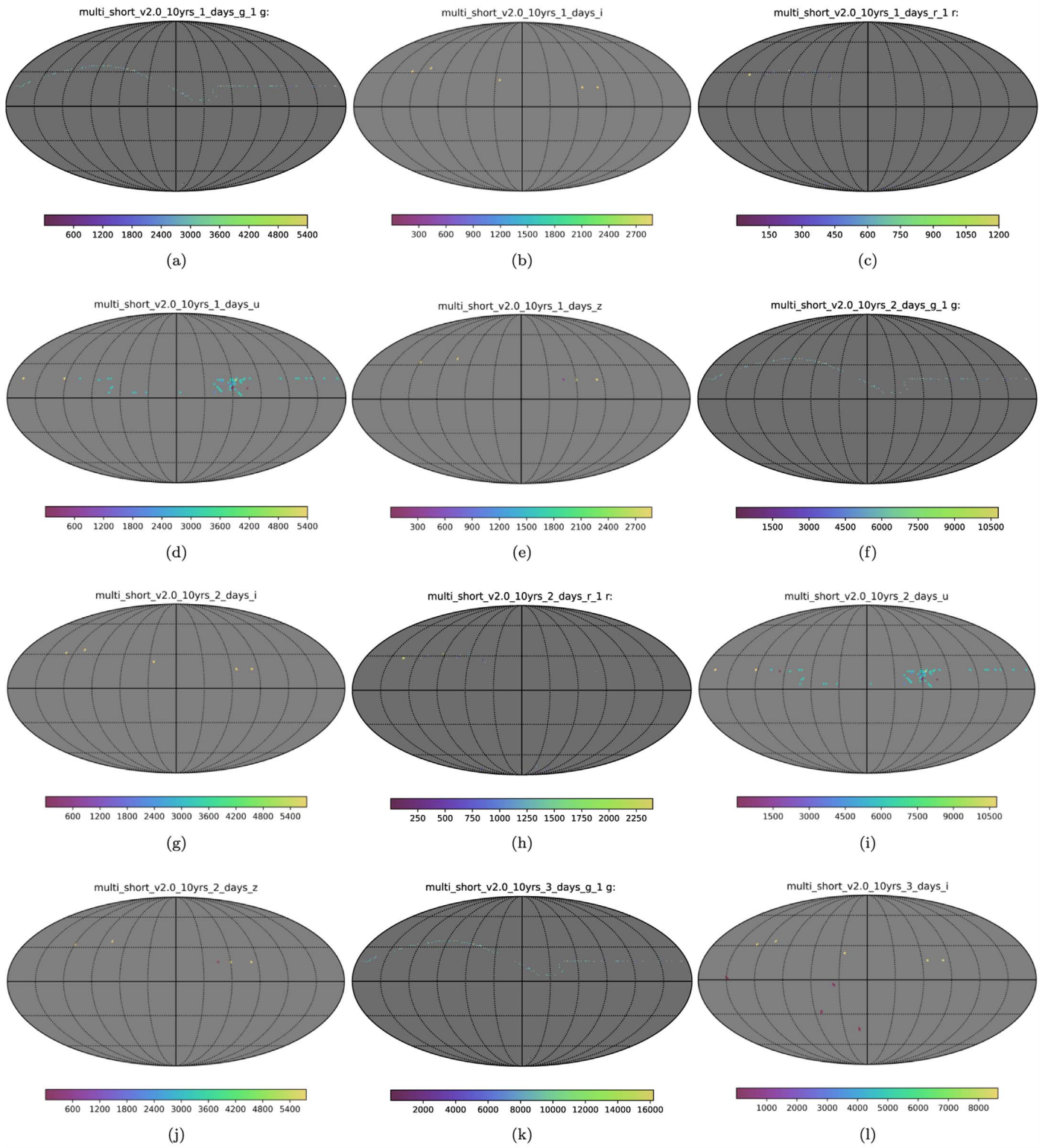


Figure A6. Metric realization on multishort cadences. DDFs appear in panel (l).

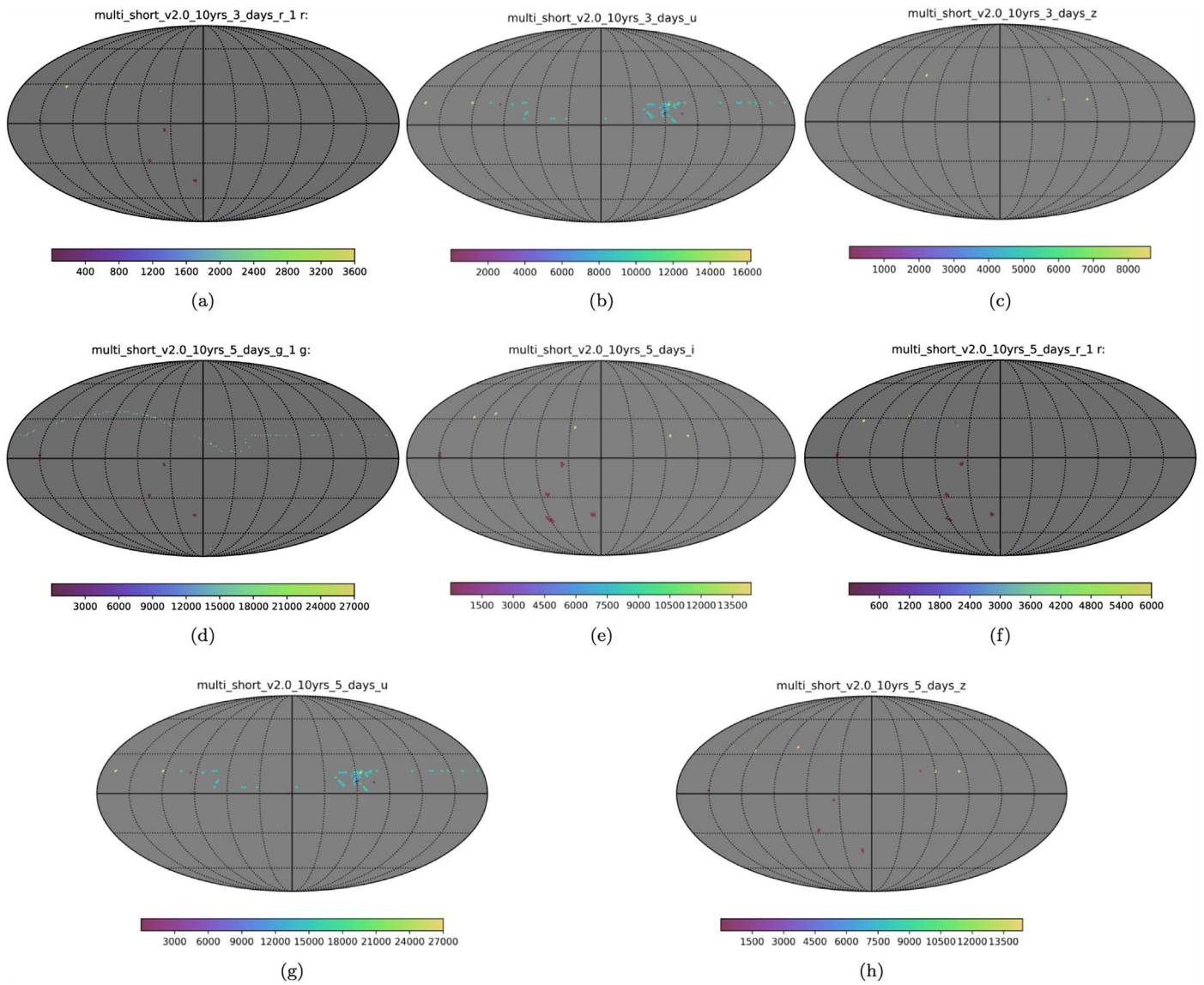


Figure A7. Metric realization on multishort cadences continued. DDFs appear in all panels except (b), (c), and (g).

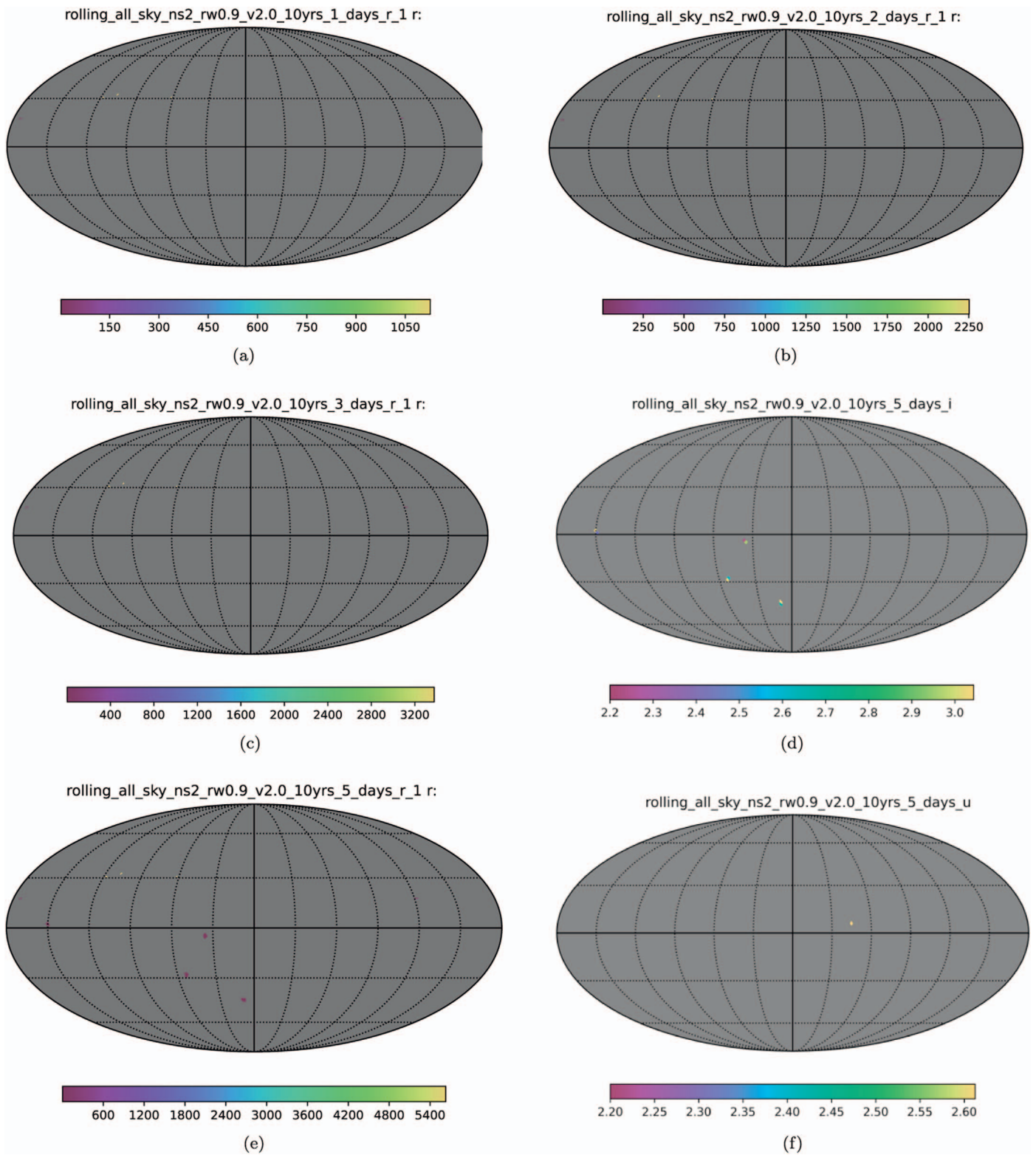


Figure A8. Metric realization on `rolling_all_sky_ns2` cadences. Panels (a)–(c) show the fields (in the fourth area from the left of the main meridian) suitable for calculating 1–3 day delays. DDFs appear in panels (d) and (e).

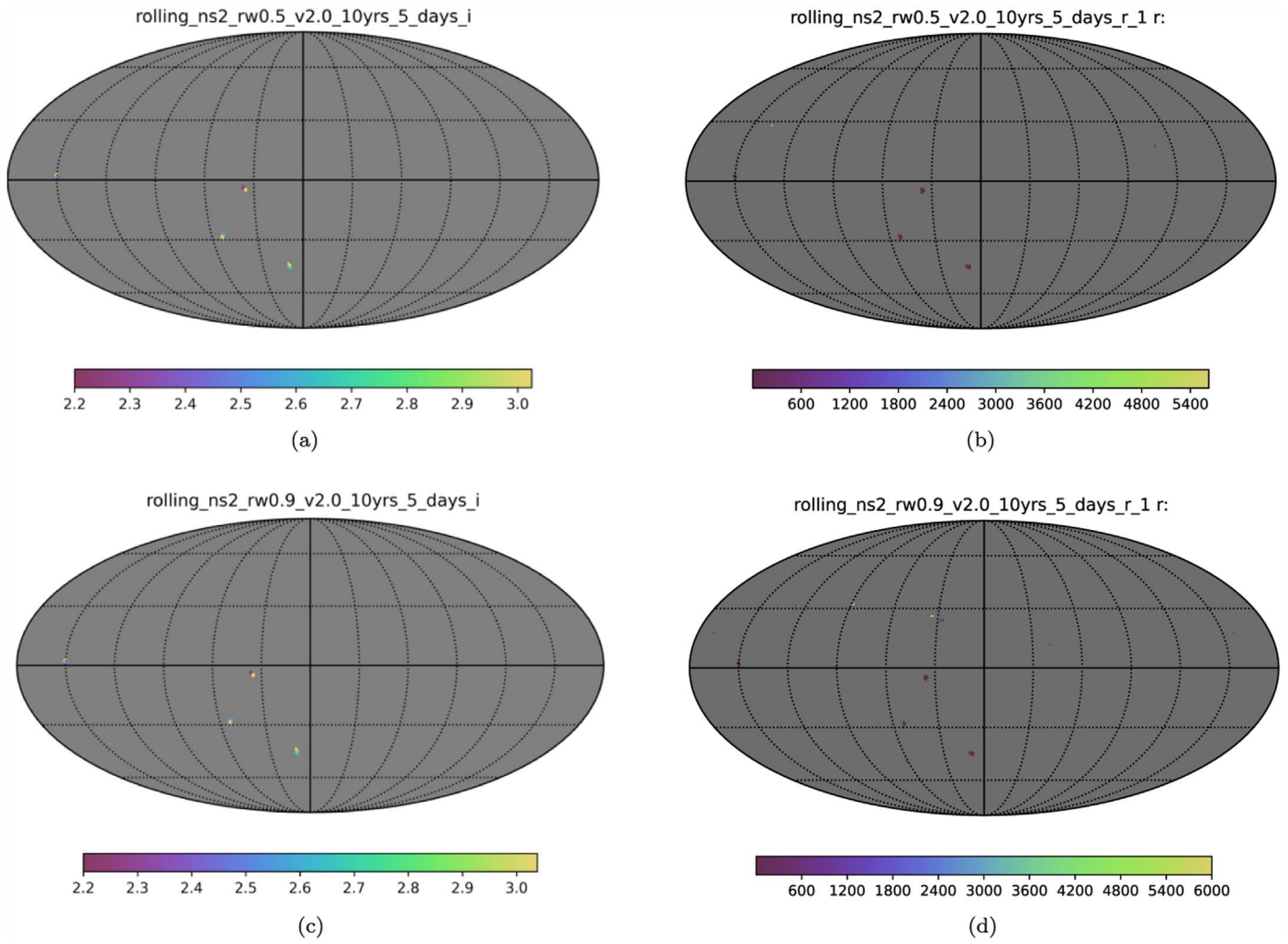


Figure A9. Metric realization on `rolling_all_sky_ns2` cadences continued. DDFs appear in all panels.

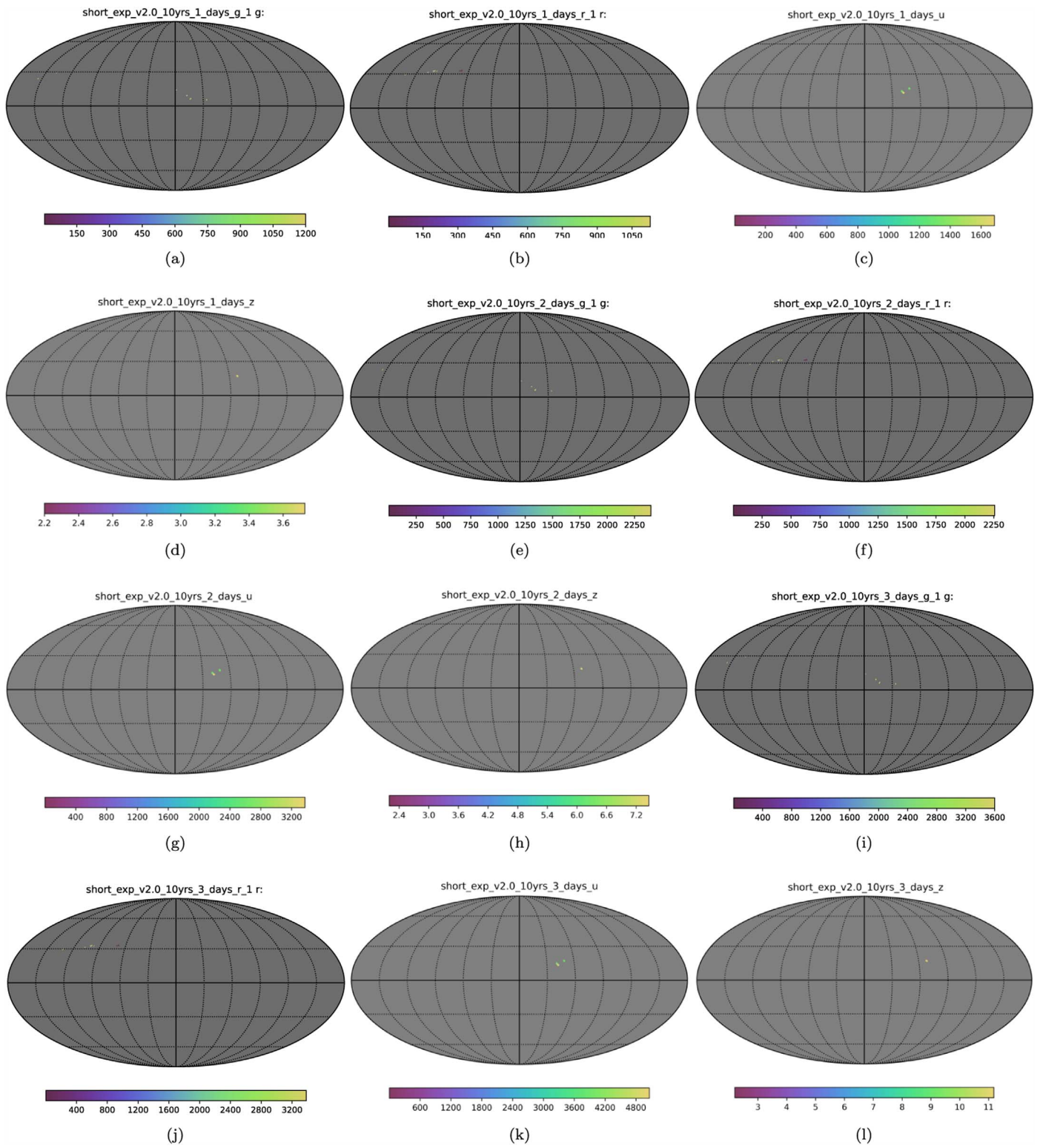


Figure A10. Metric realization on short_exp cadences. Metric run emphasizes two fields in the *u* band (panels (c), (g), and (k)).

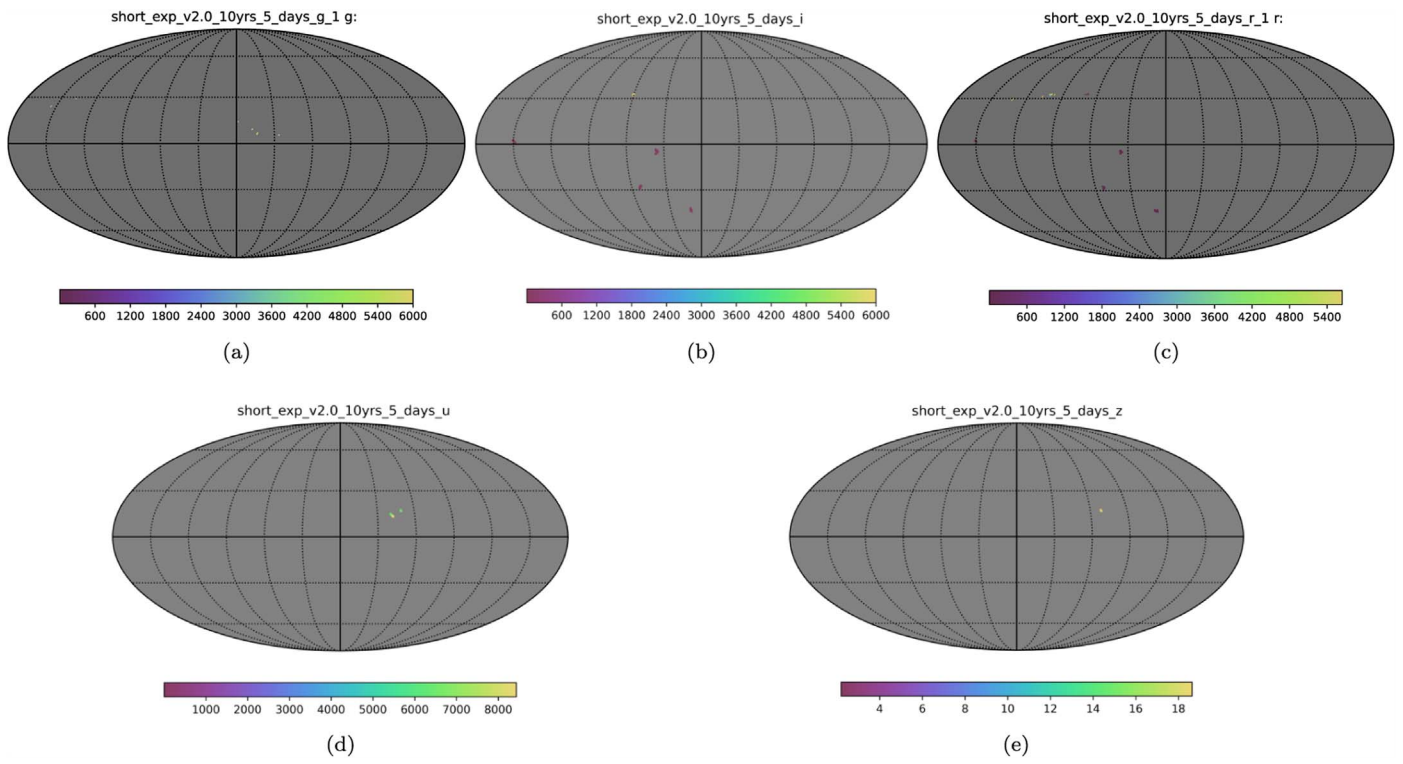


Figure A11. Metric realization on `short_exp` cadences continued. Three DDFs are prominent in panels (b) and (c).

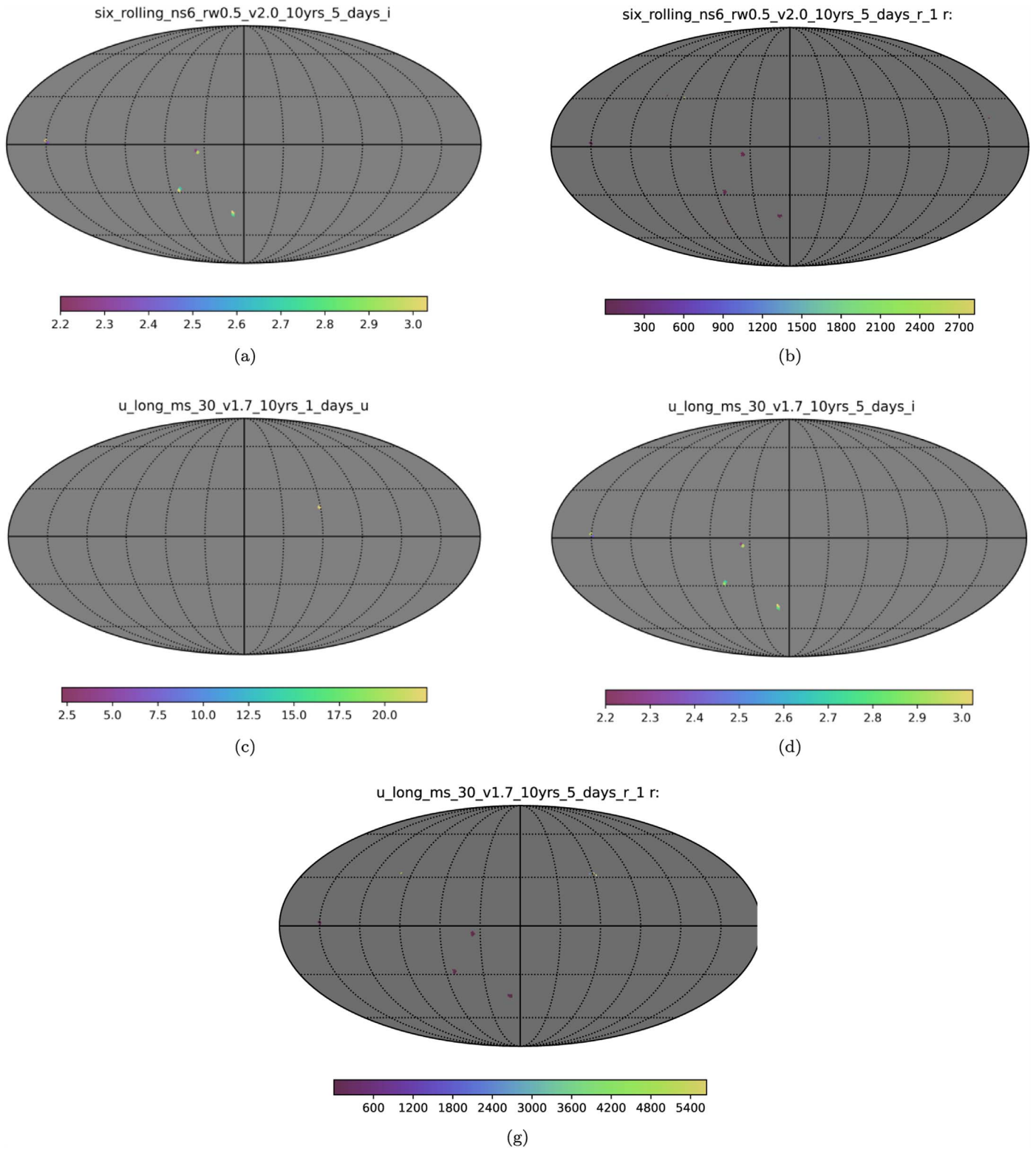


Figure A12. Metric realization on `six_rolling` and `u_long_ms_30` cadences. DDFs are prominent in the *i* band (panels (a) and (e)) and the *r* band (panels (b) and (g)).

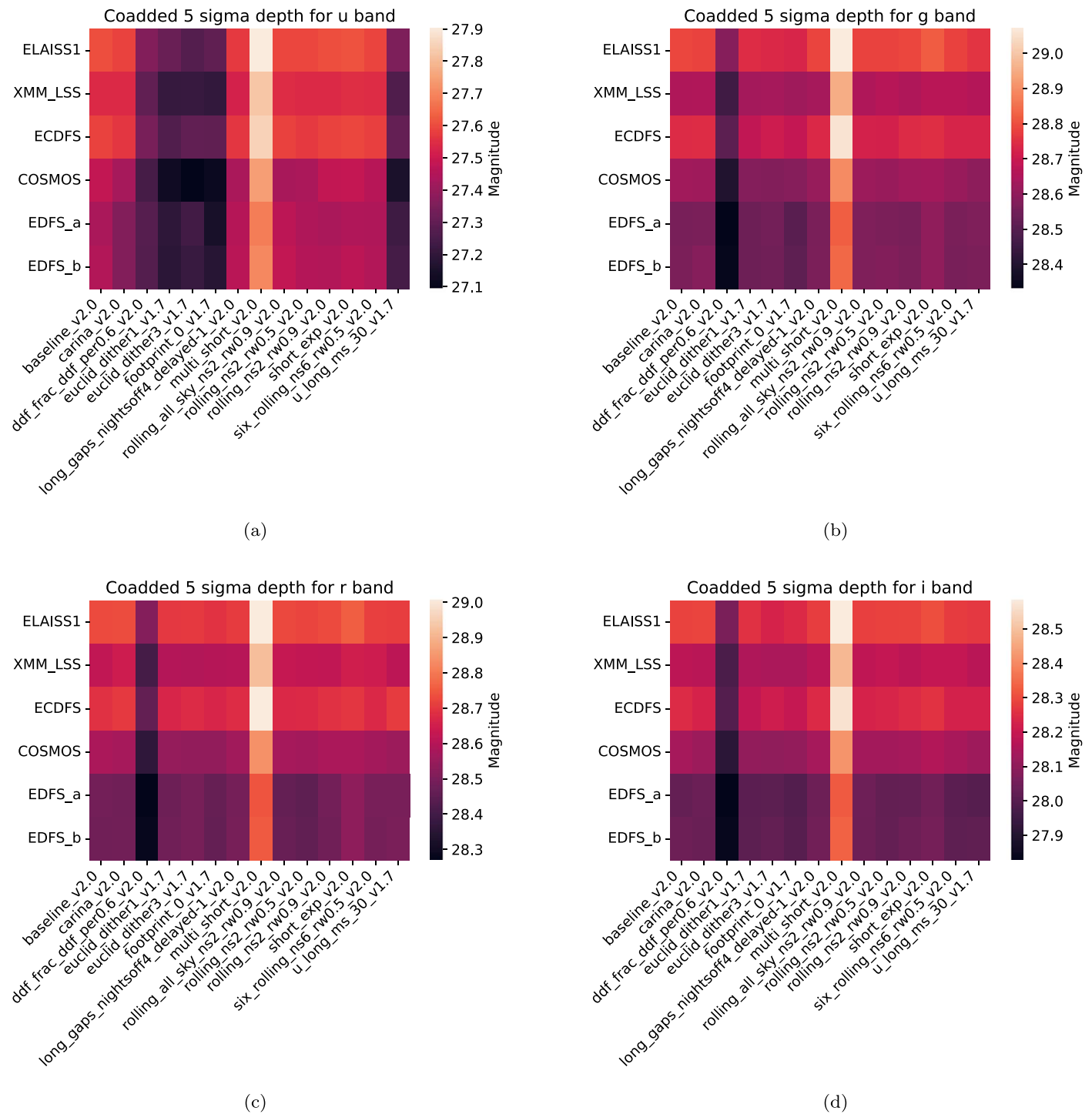
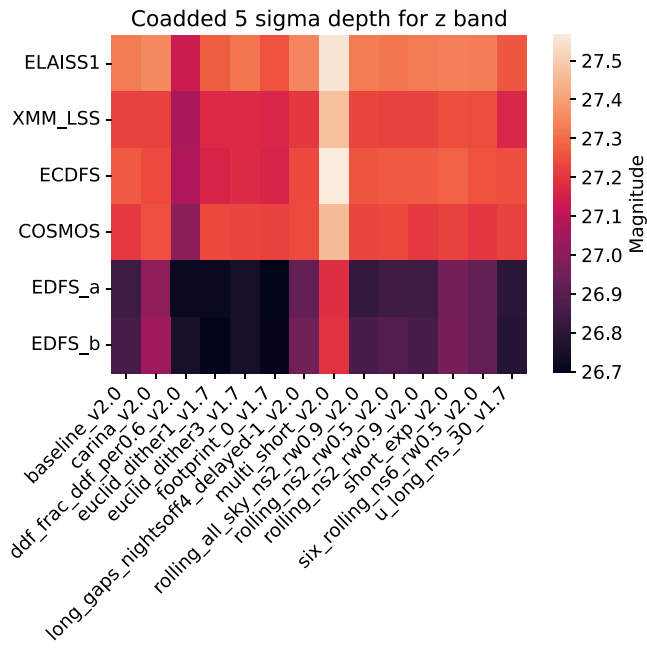
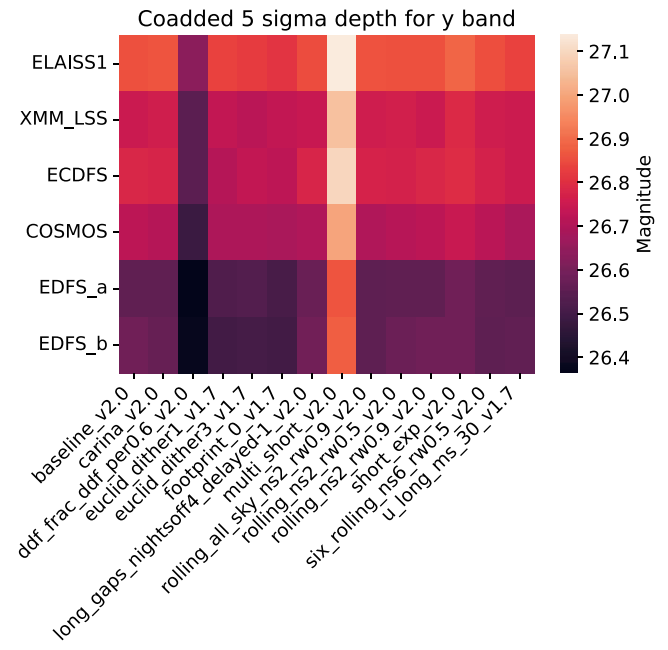


Figure A13. Coadded depth in DDFs for different observing strategies in the u, g, r, i filters. The best strategy for AD RM is also the deepest in all bands.



(e)



(f)

Figure A14. The same as Figure A13, but for the z, y filters.

ORCID iDs

Andjelka B. Kovačević  <https://orcid.org/0000-0001-5139-1978>
 Viktor Radović  <https://orcid.org/0000-0002-1172-128X>
 Dragana Ilić  <https://orcid.org/0000-0002-1134-4015>
 Luka Č. Popović  <https://orcid.org/0000-0003-2398-7664>
 Roberto J. Assef  <https://orcid.org/0000-0002-9508-3667>
 Paula Sánchez-Sáez  <https://orcid.org/0000-0003-0820-4692>
 Robert Nikutta  <https://orcid.org/0000-0002-7052-6900>
 Claudia M. Raiteri  <https://orcid.org/0000-0003-1784-2784>
 Ilsang Yoon  <https://orcid.org/0000-0001-9163-0064>
 Yasaman Homayouni  <https://orcid.org/0000-0002-0957-7151>
 Yan-Rong Li  <https://orcid.org/0000-0001-5841-9179>
 Neven Caplar  <https://orcid.org/0000-0003-3287-5250>
 Bozena Czerny  <https://orcid.org/0000-0001-5848-4333>
 Swayamrupa Panda  <https://orcid.org/0000-0002-5854-7426>
 Claudio Ricci  <https://orcid.org/0000-0001-5231-2645>
 Christian Wolf  <https://orcid.org/0000-0002-4569-016X>
 Jelena Kovačević-Dojčinović  <https://orcid.org/0000-0002-1593-707X>
 Maša Lakićević  <https://orcid.org/0000-0002-8231-0963>
 Đorđe V. Savić  <https://orcid.org/0000-0003-0880-8963>
 Saša Simić  <https://orcid.org/0000-0001-7453-2016>
 Sladjana Marčeta-Mandić  <https://orcid.org/0000-0002-9995-057X>

References

- Aihara, H., AlSayyad, Y., Ando, M., et al. 2022, *PASJ*, 74, 247
 Alexander, T. 1997, in *Astronomical Time Series*, ed. D. Maoz, A. Sternberg, & E. M. Leibowitz (Dordrecht: Kluwer), 163
 Anglés-Alcázar, D., Quataert, E., Hopkins, P. F., et al. 2021, *ApJ*, 917, 53
 Assef, R. J., Temple, M., Richards, G., Yu, W., & Bauer, F. 2021a, *LSSST AGN SC Cadence Note: Quasar Counts*, https://docushare.lsst.org/docushare/Document-37627/Quasar_Counts.pdf
 Assef, R. J., Temple, M., Richards, G., Yu, W., & Bauer, F. 2021b, *LSSST AGN SC Cadence Note: Type-I Quasar Colors in the Context of Photometric Redshifts*, https://docushare.lsst.org/docushare/dsweb/Get/Document-37628/Quasar_Colors.pdf
 Barth, A. J., Nguyen, M. L., Malkan, M. A., et al. 2011, *ApJ*, 732, 121
 Bellm, E. C., Burke, C. J., Coughlin, M. W., et al. 2022, *ApJS*, 258, 13
 Bianco, F. B., Ivezić, Ž., Jones, R. L., et al. 2022, *ApJS*, 258, 1
 Biarna, N., Brienza, M., Bonafede, A., et al. 2021, *A&A*, 650, A170
 Blandford, R. D., & Begelman, M. C. 1999, *MNRAS*, 303, L1
 Blandford, R. D., & McKee, C. F. 1982, *ApJ*, 255, 419
 Brandt, W. N., Ni, Q., Yang, G., et al. 2018, arXiv:1811.06542
 Burke, C. J., Shen, Y., Blaes, O., et al. 2021, *Sci*, 373, 789
 Cackett, E. M., Chiang, C.-Y., McHardy, I., et al. 2018, *ApJ*, 857, 53
 Cackett, E. M., Horne, K., & Winkler, H. 2007, *MNRAS*, 380, 669
 Campana, S., & Stella, L. 1995, *MNRAS*, 272, 585
 Campitiello, S., Ghisellini, G., Sbarro, T., & Calderone, G. 2018, *A&A*, 612, A59
 Capak, P., Cuillandre, J.-C., Bernardeau, F., et al. 2019, arXiv:1904.10439
 Caplar, N., Lilly, S. J., & Trakhtenbrot, B. 2017, *ApJ*, 834, 111
 Chan, J. H. H., Millon, M., Bonvin, V., & Courbin, F. 2020, *A&A*, 636, A52
 Chartas, G., Kochanek, C. S., Dai, X., et al. 2012, *ApJ*, 757, 137
 Chartas, G., Rhea, C., Kochanek, C., et al. 2016, *AN*, 337, 356
 Chelouche, D. 2013, *ApJ*, 772, 9
 Chelouche, D., & Daniel, E. 2012, *ApJ*, 747, 62
 Chelouche, D., Daniel, E., & Kaspi, S. 2012, *ApJL*, 750, L43
 Cherepashchuk, A. M., & Lyutyi, V. M. 1973, *ApL*, 13, 165
 Collier, S. J., Horne, K., Kaspi, S., et al. 1998, *ApJ*, 500, 162
 Connolly, A. J., Angeli, G. Z., Chandrasekharan, S., et al. 2014, *Proc. SPIE*, 9150, 915014
 Cuillandre, J.-C., Rhodes, J., Stern, D., et al. 2021, *LSSST Cadence Note – Enhancing LSST Science with Euclid Synergy and a Mini-survey of the Northern Sky to Dec <+30*, https://docushare.lsst.org/docushare/dsweb/Get/Document-37641/Enhancing_LSST_with_Euclid.pdf
 Čvorović Hajdinjak, I., Kovačević, A. B., Ilić, D., et al. 2022, *AN*, 343, e210103
 Dai, X., Kochanek, C. S., Chartas, G., et al. 2010, *ApJ*, 709, 278
 De Cicco, D., Bauer, F. E., Paolillo, M., et al. 2021, *A&A*, 645, A103
 Delgado, F., & Reuter, M. A. 2016, *Proc. SPIE*, 9910, 991013
 Denney, K. D., Watson, L. C., Peterson, B. M., et al. 2009, *ApJ*, 702, 1353
 Dexter, J., & Agol, E. 2011, *ApJL*, 727, L24
 Du, P., Hu, C., Lu, K.-X., et al. 2015, *ApJ*, 806, 22
 Edelson, R., Gelbord, J. M., Horne, K., et al. 2015, *ApJ*, 806, 129
 Edelson, R., Gelbord, J., Cackett, E., et al. 2017, *ApJ*, 840, 41
 Edelson, R., Gelbord, J., Cackett, E., et al. 2019, *ApJ*, 870, 123
 Event Horizon Telescope Collaboration, Akiyama, K., Alberdi, A., Alef, W., & Algaba, J. C. 2022, *ApJL*, 930, L16
 Event Horizon Telescope Collaboration, Akiyama, K., Alberdi, A., et al. 2019, *ApJL*, 875, L4
 Eyer, L., & Bartholdi, P. 1999, *A&AS*, 135, 1
 Fausnaugh, M. M., Denney, K. D., Barth, A. J., et al. 2016, *ApJ*, 821, 56
 Frank, J., King, A., & Raine, D. J. 2002, *Accretion Power in Astrophysics: Third Edition* (Cambridge: Cambridge Univ. Press)
 Galeev, A. A., Rosner, R., & Vaiana, G. S. 1979, *ApJ*, 229, 318
 Gaskell, C. M., & Peterson, B. M. 1987, *ApJS*, 65, 1
 Gaskell, C. M., & Sparke, L. S. 1986, *ApJ*, 305, 175
 Gravity Collaboration, Sturm, E., Dexter, J., et al. 2018, *Natur*, 563, 657
 Guo, W.-J., Li, Y.-R., Zhang, Z.-X., Ho, L. C., & Wang, J.-M. 2022, *ApJ*, 929, 19
 Haas, M., Chini, R., Ramolla, M., et al. 2011, *A&A*, 535, A73
 Homayouni, Y., Trump, J. R., Grier, C. J., et al. 2019, *ApJ*, 880, 126
 Hönig, S. F. 2014, *ApJL*, 784, L4
 Hopkins, P. F., Hernquist, L., Cox, T. J., et al. 2005, *ApJ*, 630, 705
 Hopkins, P. F., Richards, G. T., & Hernquist, L. 2007, *ApJ*, 654, 731
 Horne, J. H., & Baliunas, S. L. 1986, *ApJ*, 302, 757
 Hu, Z., & Tak, H. 2020, *AJ*, 160, 265
 Huber, S., Suyu, S. H., Noebauer, U. M., et al. 2019, *A&A*, 631, A161
 Ichikawa, K., Ueda, J., Bae, H.-J., et al. 2019, *ApJ*, 870, 65
 Ichimaru, S. 1977, *ApJ*, 214, 840
 Ilić, D., Oknyansky, V., Popović, L. Č., et al. 2020, *A&A*, 638, A13
 Ivezić, Ž. 2021, *Survey Cadence Optimization Committee’s Phase 1 Recommendation*, <https://docushare.lsst.org/docushare/dsweb/Get/Document-38411>
 Ivezić, Ž., Kahn, S. M., Tyson, J. A., et al. 2019, *ApJ*, 873, 111
 Jankov, I., Kovačević, A. B., Ilić, D., et al. 2022, *AN*, 343, e210090
 Jekel, C. F., Venter, G., Venter, M. P., Stander, N., & Haftka, R. T. 2019, *Int. J. Mater. Form.*, 12, 355
 Jiang, Y.-F., Green, P. J., Greene, J. E., et al. 2017, *ApJ*, 836, 186
 Jones, R. L., Yoachim, P., Chandrasekharan, S., et al. 2014, *Proc. SPIE*, 9149, 91490B
 Jones, R. L., Yoachim, P., Ivezić, Ž., Neilsen, E. H., & Ribeiro, T. 2020, *Survey Strategy and Cadence Choices for the Vera C. Rubin Observatory Legacy Survey of Space and Time (LSST) (v1.2)*, Zenodo, doi:10.5281/zenodo.4048838
 Kammoun, E. S., Papadakis, I. E., & Dovčiak, M. 2021, *MNRAS*, 503, 4163
 Kara, E., Cackett, E. M., Fabian, A. C., Reynolds, C., & Uttley, P. 2014, *MNRAS*, 439, L26
 Kara, E., Mehdipour, M., Kriss, G. A., et al. 2021, *ApJ*, 922, 151
 Kaspi, S., Smith, P. S., Netzer, H., et al. 2000, *ApJ*, 533, 631
 Kelly, B. C., Bechtold, J., & Siemiginowska, A. 2009, *ApJ*, 698, 895
 Kelly, B. C., Treu, T., Malkan, M., Pancoast, A., & Woo, J.-H. 2013, *ApJ*, 779, 187
 King, A. L., Martini, P., Davis, T. M., et al. 2015, *MNRAS*, 453, 1701
 Kollatschny, W., & Fricke, K. J. 1985, *A&A*, 146, L11
 Koratkar, A. P., & Gaskell, C. M. 1991, *ApJS*, 75, 719
 Korista, K. T., & Goad, M. R. 2001, *ApJ*, 553, 695
 Kovačević, A. B., Ilić, D., Jankov, I., et al. 2021a, arXiv:2105.12420
 Kovačević, A. B., Ilić, D., Popović, L. Č., et al. 2021b, *MNRAS*, 505, 5012
 Kozłowski, S. 2017, *A&A*, 597, A128
 Kozłowski, S., Kochanek, C. S., Udalski, A., et al. 2010, *ApJ*, 708, 927
 Landt, H., Elvis, M., Ward, M. J., et al. 2011, *MNRAS*, 414, 218
 Lawther, D., Goad, M. R., Korista, K. T., Ulrich, O., & Vestergaard, M. 2018, *MNRAS*, 481, 533
 Li, Y.-R., Wang, J.-M., & Bai, J.-M. 2016, *ApJ*, 831, 206
 Liu, H. T., Bai, J. M., Zhao, X. H., & Ma, L. 2008, *ApJ*, 677, 884
 Liu, H.-Y., Liu, W.-J., Dong, X.-B., et al. 2019, *ApJS*, 243, 21
 Lu, K.-X., Huang, Y.-K., Zhang, Z.-X., et al. 2019, *ApJ*, 877, 23
 MacLeod, C. L., Ivezić, Ž., Kochanek, C. S., et al. 2010, *ApJ*, 721, 1014

- MacLeod, C. L., Morgan, C. W., Mosquera, A., et al. 2015, *ApJ*, 806, 258
- Mastroserio, G., Ingram, A., & van der Klis, M. 2018, *MNRAS*, 475, 4027
- Mathews, T. A., & Sandage, A. R. 1963, *ApJ*, 138, 30
- McHardy, I. M., Cameron, D. T., Dwelly, T., et al. 2014, *MNRAS*, 444, 1469
- Moravec, E., Svoboda, J., Borkar, A., et al. 2022, *A&A*, 662, A28
- Morgan, C. W., Kochanek, C. S., Morgan, N. D., & Falco, E. E. 2010, *ApJ*, 712, 1129
- Morgan, C. W., Hainline, L. J., Chen, B., et al. 2012, *ApJ*, 756, 52
- Morganti, R. 2017, *NatAs*, 1, 596
- Mosquera, A. M., Kochanek, C. S., Chen, B., et al. 2013, *ApJ*, 769, 53
- Mudd, D., Martini, P., Zu, Y., et al. 2018, *ApJ*, 862, 123
- Mushotzky, R. F., Edelson, R., Baumgartner, W., & Gandhi, P. 2011, *ApJL*, 743, L12
- Netzer, H. 2013, *The Physics and Evolution of Active Galactic Nuclei* (Cambridge: Cambridge Univ. Press)
- Netzer, H. 2022, *MNRAS*, 509, 2637
- Neustadt, J. M. M., & Kochanek, C. S. 2022, *MNRAS*, 513, 1046
- O'Brien, P. T., Dietrich, M., Leighly, K., et al. 1998, *ApJ*, 509, 163
- Oknyansky, V. L., Winkler, H., Tsygankov, S. S., et al. 2019, *MNRAS*, 483, 558
- Padovani, P., Alexander, D. M., Assef, R. J., et al. 2017, *A&ARv*, 25, 2
- Panda, S. 2022, arXiv:2206.10056
- Panda, S., Czerny, B., Adhikari, T. P., et al. 2018, *ApJ*, 866, 115
- Panda, S., Martínez-Aldama, M. L., & Zajaček, M. 2019, *FrASS*, 6, 75
- Penton, A., Malik, U., Davis, T. M., et al. 2022, *MNRAS*, 509, 4008
- Peterson, B. M. 2006, in *Physics of Active Galactic Nuclei at All Scales*, ed. D. Alloin et al. (Berlin: Springer), 77
- Peterson, B. M., Ferrarese, L., Gilbert, K. M., et al. 2004, *ApJ*, 613, 682
- Pooley, D., Blackburne, J. A., Rappaport, S., & Schechter, P. L. 2007, *ApJ*, 661, 19
- Pooley, D., Blackburne, J. A., Rappaport, S., Schechter, P. L., & Fong, W.-F. 2006, *ApJ*, 648, 67
- Poutanen, J., & Beloborodov, A. M. 2006, *MNRAS*, 373, 836
- Pozo Nuñez, F., Gianniotis, N., Blex, J., et al. 2019, *MNRAS*, 490, 3936
- Pozo Nuñez, F., Ramolla, M., Westhues, C., et al. 2015, *A&A*, 576, A73
- Press, W. H., Teukolsky, S. A., Vetterling, W. T., & Flannery, B. P. 1992, *Numerical Recipes in C. The Art of Scientific Computing* (Cambridge: Cambridge Univ. Press)
- Raiteri, C. M., Carnerero, M. I., Balmaverde, B., et al. 2022, *ApJS*, 258, 3
- Reuter, M. A., Cook, K. H., Delgado, F., Petry, C. E., & Ridgway, S. T. 2016, *Proc. SPIE*, 9911, 991125
- Roberts, D. H., Lehar, J., & Dreher, J. W. 1987, *AJ*, 93, 968
- Sahu, N., Graham, A. W., & Davis, B. L. 2019a, *ApJ*, 887, 10
- Sahu, N., Graham, A. W., & Davis, B. L. 2019b, *ApJ*, 876, 155
- Sánchez-Sáez, P., Lira, P., Mejía-Restrepo, J., et al. 2018, *ApJ*, 864, 87
- Scargle, J. D. 1982, *ApJ*, 263, 835
- Schmidt, M. 1963, *Natur*, 197, 1040
- Scolnic, D. M., Lochner, M., Gris, P., et al. 2018, arXiv:1812.00516
- Sergeev, S. G., Doroshenko, V. T., Golubinskiy, Y. V., Merkulova, N. I., & Sergeeva, E. A. 2005, *ApJ*, 622, 129
- Shakura, N. I., & Sunyaev, R. A. 1973, *A&A*, 500, 33
- Shappee, B. J., Prieto, J. L., Grupe, D., et al. 2014, *ApJ*, 788, 48
- Shemmer, O., Richards, G., Brandt, N., et al. 2018, LSST AGN Science Collaboration Roadmap, https://agn.science.lsst.org/sites/default/files/LSST_AGN_SC_Roadmap_v1p0.pdf
- Shen, X., Hopkins, P. F., Faucher-Giguère, C.-A., et al. 2020, *MNRAS*, 495, 3252
- Shen, Y., Richards, G. T., Strauss, M. A., et al. 2011, *ApJS*, 194, 45
- Smith, K. L., Mushotzky, R. F., Boyd, P. T., et al. 2018, *ApJ*, 857, 141
- Srinivasan, R., Tucker, D. M., & Murias, M. 1998, *Behav. Res. Methods, Instrum. Comput.*, 30, 11
- Starkey, D., Horne, K., Fausnaugh, M. M., et al. 2017, *ApJ*, 835, 65
- Starkey, D. A., Horne, K., & Villforth, C. 2016, *MNRAS*, 456, 1960
- Stone, Z., Shen, Y., Burke, C. J., et al. 2022, *MNRAS*, 514, 164
- Suberlak, K. L., Ivezić, Ž., & MacLeod, C. 2021, *ApJ*, 907, 96
- Sun, W.-H., & Malkan, M. A. 1989, *ApJ*, 346, 68
- Tachibana, Y., Graham, M. J., Kawai, N., et al. 2020, *ApJ*, 903, 54
- Tekhanovich, D. I., & Baryshev, Y. V. 2016, *AstBu*, 71, 155
- Tewes, M., Courbin, F., & Meylan, G. 2013, *A&A*, 553, A120
- Thater, S., Krajnović, D., Cappellari, M., et al. 2019, *A&A*, 625, A62
- Thorne, K. S. 1974, *ApJ*, 191, 507
- Vasudevan, R. V., Mushotzky, R. F., Winter, L. M., & Fabian, A. C. 2009, *MNRAS*, 399, 1553
- Yu, W., & Richards, G. 2021, LSST AGN SC Cadence Note: Non-Parametric Structure Function Metric, https://docushare.lsst.org/docushare/dsweb/Get/Document-37656/AGN_SF_Metric.pdf
- Yu, W., Richards, G. T., Vogeley, M. S., Moreno, J., & Graham, M. J. 2022, *ApJ*, 936, 132
- Yu, Z., Martini, P., Davis, T. M., et al. 2020, *ApJS*, 246, 16
- Yuan, F., & Narayan, R. 2014, *ARA&A*, 52, 529
- Zou, F., Brandt, W. N., Chen, C.-T., et al. 2022, *ApJS*, 262, 15
- Zu, Y., Kochanek, C. S., Kozłowski, S., & Peterson, B. M. 2016, *ApJ*, 819, 122
- Zu, Y., Kochanek, C. S., Kozłowski, S., & Udalski, A. 2013, *ApJ*, 765, 106
- Zu, Y., Kochanek, C. S., & Peterson, B. M. 2011, *ApJ*, 735, 80
- Zubovas, K., & King, A. 2021, *MNRAS*, 501, 4289